COUPLING OF ACID FRACTURE AND RESERVOIR IN CARBONATE RESERVOIRS UNDER NON-ISOTHERMAL CONDITION

A Thesis

by

TOHOKO TAJIMA

Submitted to the Office of Graduate and Professional Studies of
Texas A&M University
in partial fulfillment of the requirements for the degree of

MASTER OF SCIENCE

Chair of Committee,	Ding Zhu
Committee Members,	A. Dan Hill
	Zachary Gagnon
Head of Department,	Jeff Spath

August 2020

Major Subject: Petroleum Engineering

ABSTRACT

Modeling acid fracturing process is challenging because of the coupled complex effects of flow through porous medium and fracture, chemical reaction in a geostatistic base, wormhole propagation and reservoir heterogeneity. To avoid the complexity, decoupled approaches are commonly used, and often the reservoir effect is represented by leakoff effect with a constant leakoff coefficient. An acid fracturing numerical model is presented that is coupled with a single-phase black oil reservoir simulator for a vertical well in carbonate reservoir. To analyze the benefits of coupled modeling, a comparison is performed with a conventional acid fracturing model that is decoupled from reservoir model.

The coupled acid fracturing model considers fracture propagation and closure, acid transport, and heat transfer. After simulate acid fracturing, conductivity of the fracture is calculated using empirical correlations, and the productivity is computed by simulating the flow to the well. Non-isothermal condition is assumed to simulate the flow in both fracture and reservoir because the acid reaction temperature sensitive. Leakoff from fracture to reservoir is simulated with a reservoir flow model for pressure and leakoff velocity as functions of time and location. Wormhole propagation from the fracture is considered by using empirical equations for wormhole propagation based on leakoff velocity estimated from the reservoir simulation. Governing equations and computation procedure used to develop the model are illustrated in the paper with details.

Comparisons of the coupled and decoupled acid fracturing models are performed. The results show that the coupling reservoir model improves the estimated in fracture conductivity. A case study is presented to illustrate the significance of coupling process in simulation of acid fracturing. The effect of wormholing on acid fracture conductivity is also investigated. Wormhole propagation causes high leakoff at the entrance of the fracture and results in higher conductivity at the fracture entrance. The wormhole propagation has little effect on fracture geometry and acid penetration distance. It is concluded based on the observation of the study that the leakoff from acid fracture represented by reservoir model with wormhole propagation is important to correctly understand acid fracture efficiency. Simply using a constant leakoff coefficient can lead to significant error and misleading conclusions.

DEDICATION

To my family.

ACKNOWLEDGEMENTS

I would like to thank my advisers, Dr. Zhu and Dr. Hill for their patience, guidance and support throughout the course of this research.

I would like to thank Dr. Gagnon for serving as my committee member and the meaningful and valuable lecture in transport phenomena.

Finally, thanks to my colleagues and friends for discussions, kindness, and making my school life fun.

CONTRIBUTORS AND FUNDING SOURCES

Contributors

This work was supervised by a thesis committee consisting of Professor Zhu and Hill of the Department of Petroleum Engineering and Professor Gagnon of the Department of Chemical Engineering.

The code depicted in Chapter 2 Section 10 was developed by Mateus Palharini Schwalbert of the Department of Petroleum Engineering.

All other work conducted for the thesis was completed by the student independently.

Funding Sources

Graduate study was supported by a fellowship from Texas A&M University. This work was also made possible in part by Acid Stimulation Research Project.

NOMENCLATURE

A	Coefficient in fracture conductivity correlations
a	Geothermal gradient
B	Coefficient in fracture conductivity correlations
b	Ambient temperature
C	Acid concentration
$\tilde{C}$	Average acid concentration
C_{inj}	Injection concentration
C_L	Total leakoff coefficient
C_v	Leakoff coefficient component due to viscous filtrate invasion
C_c	Leakoff coefficient component due to reservoir fluids compression
C_w	Leakoff coefficient component due to filter cake
C_B	Acid concentration at the fracture wall
C_{eqm}	Equilibrium acid concentration
c_{ma}	Heat capacity of matrix
$c_{p,f}$	Heat capacity of reservoir fluid
$c_{p,r}$	Heat capacity of rock
c_t	Total compressibility of the reservoir fluid
D_e	Diffusion coefficient of acid
$D_{e,ref}$	Diffusion coefficient of acid at reference temperature
$dA(\tau)$	Area of the fracture surface where acid leaks off

E	Young's modulus
E'	Plane strain modulus
E_f	Reaction rate constant
E_{f0}	Coefficient in the Arrhenius formula
$\Delta E/R$	Coefficient appears in the reaction rate correlation
$f(t)$	Ramey time function, dimensionless
f_l	Fraction of leaking acid which react at the fracture wall
G	Bulk shear modulus of formation $G = \frac{E}{2(1+\nu)}$
G_n	Coefficients corresponding to eigenvalues in analytical solution for acid concentration (Nierode and Williams, 1971)
$g_{i,n}$	Coefficients in analytical solution for acid concentration (Nierode and Williams, 1971)
$H_{reaction}$	Reaction heat
ΔH	Flow activation energy per mole (Christiansen et.al.)
h	Reservoir height
h_T	Convection film transfer coefficient
h_f	Fracture height
K	Consistency index
K_g	Parametric apparent mass-transfer coefficient
k	Permeability
k_{fil}	Permeability of filtrate zone
k_{cake}	Permeability of mud cake
$k_f w$	Fracture conductivity

k_f	Fracture permeability
L_x	Reservor length
L_y	Reservor width
M_{HCl}	Molar mass of HCl
m	Constant coefficient in consistency index correlation
m_c	Reaction order of calcite
m_d	Reaction order of dolomite
N_{Pe}	Peclet Number
N_{Re}	Reynolds number in fracture length direction
N_{Re}^*	Reynolds number in fracture width direction
N_{nu}	Nusselt number
n	Power-law exponent
p	Pressure
p_d	Dimensionless pressure
p_{hf}	Fracture pressure
p_{LO}	Leakoff pressure from the hydraulic fracture
p_{res}	Reservoir pressure
p_{wf}	Wellbore flowing pressure
Δp	Pressure drop
Δp_{cake}	Pressure drop in the mud cake
Δp_{fil}	Pressure drop in filtrate zone
q_{inj}	Injection rate

q'_{inj}	Injection rate for one wing
$q_{leak,i}$	Leakoff rate at i-th grid block
$\Delta q_{in,i}$	Net influx rate at i-th grid block.
R	Gas constant
r_1	Inside radius of tubing
r_2	Outside radius of casing
S	Normal compressive stress on fracture plane before fracturing
T	Temperature
T_0	Injected fluid surface temperature
T_e	Temperature of the earth
T_{hf}	Fluid temperature in the fracture
T_{inj}	Fluid temperature at the fracture inlet
T_{ref}	Reference temperature
T_{res}	Reservoir temperature
t	Time
t_a	Time from when the acid injection started
U_t	Overall heat transfer coefficient
ΔV_{acid}	Volume of acid used to dissolve the rock
V_f	Volume of fracture
$V_{injected}$	Total injection volume of fracturing fluid
$V_{leakoff}$	Total volume leaked off from the fracture
V_{rock}	Volume of rock dissolved by acid

v	Fluid velocity
$\tilde{v}_f$	Fluid velocity in the fracture averaged in width direction
v_l	Leakoff rate
w	Fracture width
$\widetilde{w}$	Average fracture width in height direction.
w_e	Etched width
w_{max}	Maximum fracture width in height direction
$w_{max,0}$	Maximum fracture width at the wellbore
wk_f	Conductivity of fracture
X	Constant in the Elsharkawy dead oil viscosity correlation (1999)
X_f	Fracture length
Δx_{hf}	Length of grid block in x direction in fracture
Z	Coefficient appear in Ramey's equation
z	Depth

Greek

α	(1) Thermal diffusivity of the earth
α	(2) Ratio of the leakoff volume to the filtrate thickness
β	Dissolving power
$\dot{\gamma}$	Shear rate
γ_{API}	API gravity
λ_{eff}	Effective thermal conductivity

λ_f	Thermal conductivity of acid
λ_{ma}	Matrix permeability
λ_n	Eigenvalues in analytical solution for acid concentration (Nierode and Williams, 1971)
μ	Viscosity
μ_a	Viscosity of acid
μ_{ref}	Reference viscosity
μ_{app}	Apparent viscosity for power-law fluid
μ_{od}	Dead oil density
μ_{fil}	Viscosity of the filtrate
ξ	Dimensionless length along the fracture
ν	Poisson's ratio
ρ	Density
ρ_a	Density of acid
ρ_{ma}	Density of matrix
τ	(1) Shear stress
τ	(2) Time when fracturing fluid start to contact to the fracture surface
ϕ	Porosity
χ	Volumetric dissolving power

Subscript

a	Acid

fil	Filtrate zone
hf	Fracture
$cake$	Mud cake
ma	Matrix
l	Leakoff
c	Calcite
d	Dolomite
ref	Reference
x	Fracture length direction
y	Fracture width direction

TABLE OF CONTENTS

Page

LIST OF FIGURES

Page

LIST OF TABLES

Page

1. INTRODUCTION

1.1. Introduction of Acid Fracturing and Carbonate Reservoirs

Acid fracturing is a stimulation technique used in carbonate reservoirs. Acid is injected into the formation with an injection pressure higher than the fracture pressure of the formation, and create a fracture to increase the flow mobility of the formation. In general, carbonate reservoirs which have more than 65% solubility to acid can be a candidate of acid fracturing. Carbonate reservoir mainly consists of calcite [CaCO3], dolomite [CaMg(CO3)2], and evaporate minerals such as anhydrite [CaSO4]. Hydrochloric acid, formic acid, acetic acid, or a blended acid is commonly used as a stimulation fluid (Kalfayan, 2008).

The process of acid fracturing can be divided into three steps: fracture creation, acid reaction with rock, and fracture closure. First, a high viscosity fluid called pad is injected with a high injection pressure to break the formation. The fracture geometry created at this process depends on the formation properties and pad fluid properties. After the pad injection, acid is injected to react the fracture surface. The purpose of this process is to create rough fracture surfaces which provides flow path even after the fracture is closed by closure stress. Thus, acid should penetrate as deep as possible to create a rough surface in larger region. Acid penetration distance in the fracture depends on fracture geometry, acid properties, and the reaction properties between acid and rock. Finally, when fluid injection is stopped, the fracture closes due to high formation pressure. After

the cease of fluid injection, the roughness on both sides of the fracture surfaces holds the aperture and retain fracture conductivity.

A significant proportion of the world's petroleum reservoirs (about 60 percent of oil and 40 percent of gas reservoirs) in the world are found in carbonate rock reservoir (Akbar, 2000). They are mainly located in the Middle East, Libya, Russia, Kazakhstan, and North America.

Even though the carbonate reservoirs are rich in hydrocarbons, its evaluation and stimulation is much more complicated than siliciclastic reservoir. One of the reason for this is that the heterogeneity of reservoir properties is caused by not only deposition but also diagenesis. The heterogeneity of parameters can be seen in all scales from pore scale to reservoir scale, and thus the modeling of carbonate reservoir is much complicated than modeling sandstone reservoirs (Shepherd, 2009). In terms of acid fracturing, the heterogeneity of minerals have an important role since it contributes to create rough surface and thus create conductivity.

1.2. Research Objective

While there have been many studies on acid fracturing numerical modeling, few of them have focused on the interaction between the fracture and reservoir. However, since carbonate reservoirs are generally highly heterogeneous, it is important to couple a reservoir numerical model instead of using analytical solutions to consider the interaction with reservoir.

This research focuses on coupling the reservoir model to the acid fracturing simulator which considers the pressure, temperature, acid transport, and fracture propagation. Furthermore, the effect of coupling acid fracturing model with fracture propagation and reservoir model was investigated using the developed model.

Temperature has a significant impact on the acid fracturing treatment since acid reactivity and diffusivity depends on temperature, and acid reaction with rock is exothermic reaction.

The model developed in this study obtain the heat from the reservoir numerically, and it accounts for the transient effect of the fracture geometry. The effect of those simplifications is analyzed with the simulation model developed.

Wormholes which is created close to the acid fracture entrance cause the excess leakoff and reduce the fracture pressure. To evaluate the significance of the wormhole, the leakoff distribution along the fracture is investigated.

1.3. Literature Review

1.3.1. Fracture Geometry

There are two main streams of fracture propagation models; two-dimensional models and pseudo-three-dimensional models.

Two-dimensional models assume one of the dimensions constant to obtain the geometry analytically. Figure 1-1 shows the schematic of the most common models; PKN (Perkins and Kern, 1961; Nordgren, 1989) , KGD (Khristianovic and Zheltov, 1955; Geertsma and de Klerk, 1969), and radial model (Geertsma and de Klerk, 1969). PKN and

KGD model assume the fracture height is constant since the stress difference between pay zone and confining formations is significant, and the fracture does not propagate in the confining formations. In reality, however, the hydraulic fracture propagates to the upper and lower confining layers, and the height growth is important for the fracture design because one of the objectives of fracturing is to increase the vertical permeability by fracturing. Radial model considers the fracture propagates radially.

PKN model is developed by Perkins and Kern (1961) and improved by Nordgren (1989). This model assumes the fracture height is constant, and the cross-sectional area of the fracture has an elliptical shape. The maximum and average fracture width for Newtonian fluid are derived from the Fanning equation and the fracture width equation under internal pressure shown by Sneddon (1946):

$$w_{max} = 3.27\left[\frac{q_i \mu X_f}{E'}\right]^{1/4} \tag{1.1}$$

$$\widetilde{w} = 0.19\left[\frac{q_i \mu X_f}{E'}\right]^{1/4} \tag{1.2}$$

As it is indicated in Eq.(1.1) and (1.2), the fracture length is required to calculate the width. The fracture length can be calculated from the material balance in the fracture. The material balance equation is derived by equating the injected fluid volume to the sum of the leakoff volume and the fracture volume increase, and it will be cubic equation.

KGD model is also based on Sneddon's (1946) fracture width equation, but it is applied in perpendicular direction, while PKN model applied it in horizontal direction.

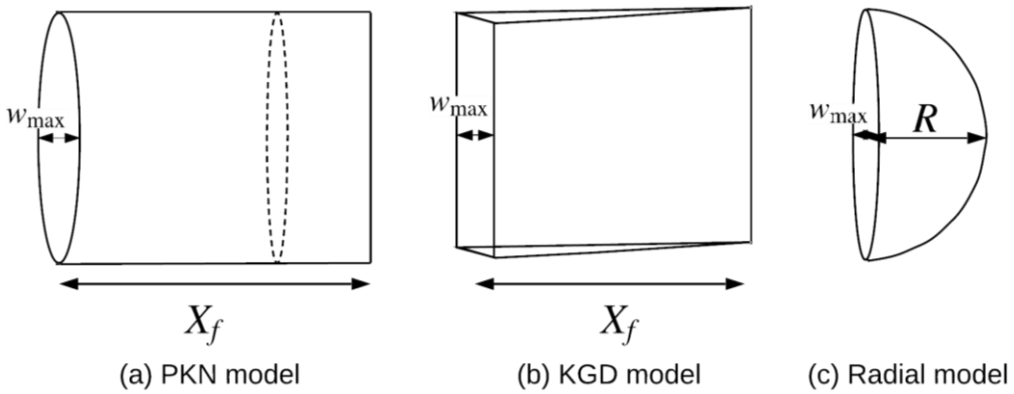

Figure 1-1 Fracture shapes of 2D analytical models: PKN, KGD, and radial model

In addition to width and length growth of the fracture, pseudo-3D (P3D) models allow to consider height growth in multiple layers. Simonson (1978) proposed a simple model for fracture height growth in a reservoir with upper and lower overlaying layers. This model can be incorporated with GDK and PKN models to optimize fracture design. P3D models for more complicated situations have been developed such as more than three layers. (Cleary, 1980; Meyer, 1986; Liu and Valko, 2015).

1.3.2. Acid Transport and Reaction in Fracture

When acid is injected in a fracture, it reacts with the fracture wall. The reaction is based on the stoichiometry relationship between acid and carbonate rock. Common acid used is hydrochloric acid [HCl], formic acid [HCOOH], acetic acid [CH_3COOH], or a blend of those. Those acids react with soluble minerals in carbonate rock such as calcite [$CaCO_3$] and dolomite [$CaMg(CO_3)_2$]. The reaction of those minerals with hydrochloric acid can be written in chemical formula as follows:

$$2HCl + CaCO_3 \rightarrow CaCl_2 + H_2O + CO_2 \qquad (1.3)$$

$$4HCl + CaMg(CO_3)_2 \rightarrow CaCl_2 + MgCl_2 + 2H_2O + 2CO_2 \qquad (1.4)$$

1.3.3. Leakoff during Acid Fracturing

One of the crucial parameters for acid fracturing performance is a fluid loss rate. Fluid loss from an acid fracture in carbonate reservoir is generally much more difficult to control than a propped fracture in sandstone since acid continually dissolves the rock. Besides, most of carbonate reservoirs are naturally fractured and they are much harder to plug with additives.

The classic leakoff model was introduced by Carter (1957), which is derived from the one-dimensional continuity equation for a slightly compressible fluid. The equation is described as follows;

$$q_L = \frac{2C_L dA(\tau)}{\sqrt{t-\tau}} \qquad (1.5)$$

where C_L is total leakoff coefficient, $dA(\tau)$ is an area of the fracture surface where acid leaks off, t is time, and τ is the time when fracturing fluid start to contact to the fracture surface.

According to Settari (1985), the total leakoff coefficient, C_L consists of the effect of three separate regions; filter cake, filtrate zone, and reservoir zone. The effect of each regions can likewise be expressed as a form of leakoff coefficient. The relationship between total leakoff coefficient and that of each region is:

$$\frac{1}{C_L} = \frac{1}{C_v} + \frac{1}{C_c} + \frac{1}{C_w} \qquad (1.6)$$

where C_v, C_c, and C_w stand for the leakoff coefficient components due to viscous filtrate invasion, reservoir fluids compression, and filter cake, respectively. Those coefficients are calculated from the following equations:

$$C_v = \sqrt{\frac{k_{fil}\phi\Delta p_{fil}}{2\mu_{fil}}} \tag{1.7}$$

$$C_c = \sqrt{\frac{\phi k_{res} c_t}{\pi\mu}}\left(p_{hf} - p_{res}\right) \tag{1.8}$$

$$C_w = \sqrt{\frac{k_{cake}\alpha\Delta p_{cake}}{2\mu_{fil}}} \tag{1.9}$$

where k_{fil} is the permeability of filtrate zone, ϕ is the porosity of reservoir, Δp_{fil} is the pressure drop in the filtrate zone, k_{res} is the reservoir permeability, μ_{fil} is the viscosity of filterate, c_t is the total compressibility of the reservoir fluid, p_{hf} is the fracture pressure, p_{res} is the reservoir pressure, k_{cake} is the permeability of mud cake, α is a ratio of the leakoff volume to the filtrate thickness, Δp_{cake} is the pressure drop in the mud cake.

When the effect of mud cake can be ignored, the relationship can be simplified as follows:

$$C_L = \frac{2C_v C_c}{C_v + \sqrt{{C_v}^2 + 4{C_c}^2}} \tag{1.10}$$

It is common to ignore the effect of filter cake in acid fracturing, since the acid dissolves the mud cake.

1.3.4. Wormholes

When acid passes through the heterogeneous porous media, acid tends to go to the least resistive path and dissolves the surface of the pore as it passes through. As acid dissolves the pore surface and enlarge the pore, the least resistive path becomes less resistive, and thus more acid flows to this path. The highly permeable flow path created by this procedure is known as a wormhole. Figure 1-2 shows the CT images of wormholes with different acid injection volume (Darren, 2010). The wormhole development on the fracture surface sometimes hurts the acid fracturing because too much acid leakoff from wormholes and the fracture cannot maintain the fluid pressure higher than the fracture pressure.

Leakoff models which account for wormhole propagation from acid fracture surfaces have been proposed.

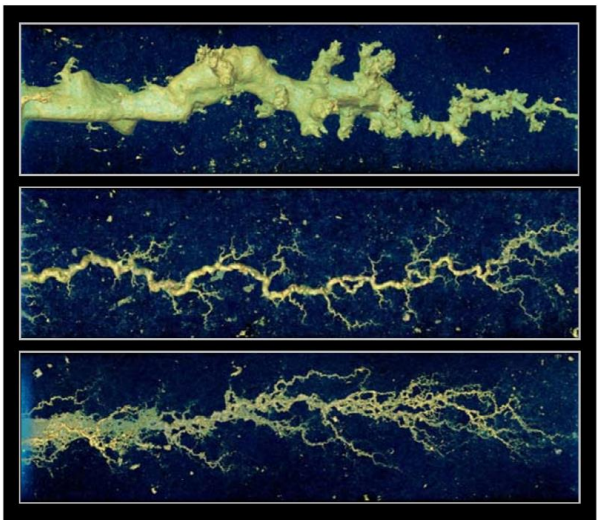

Figure 1-2 High-Resolution CT Images of Acidized Core Plugs (Darren, 2010)

Hill et al. (1995) extended Carter's equation to include the effect of wormholes by reformulating the leakoff coefficient for the invaded zone. This model is valid when the wormhole propagation is not efficient, thus the optimum pore volume to breakthrough is larger than 1. This situation happens when the formation has low permeability, consists of dolomite formations, or is stimulated by weak acid. However, when strong acids such as hydrochloric acid are used, the wormhole propagation tends to be more effective (the optimum pore volume to breakthrough is less than 1).

Schwalbert (2019) developed a leakoff model which considers the effect of wormholes when the optimum pore volume to breakthrough is less than 1. He incorporated his wormhole model into a fully integrated acid fracturing model developed by Al Jawad (2018). Comparing the result from this model to that of an acid fracturing model without leakoff model, he concluded that the presence of wormholes in the acid fracture is only important when the productivity index of matrix acidizing is higher than acid fracturing.

1.3.5. Heat Transfer in Acid Fracture

Temperature has an significant effect on the result of acid fracturing since the acid reactivity, diffusivity, and viscosity depend on temperature. It is invalid to assume the fracturing fluid is at formation temperature because the injection fluid reaches a perforation at temperature nearly the same as the surface injection temperature. The cooler temperature generally has a positive effect on acid fracturing, because it reduces the acid reactivity and helps to increase the acid penetration distance.

The simplest analytical solution for temperature in a fracture is proposed by Whitsitt and Dysart (1970). Their model is derived by solving the energy balance equation and mass balance equation.

Lee and Roberts (1980) improved Whitsitt and Dysart (1970) model to apply it on acid fracturing by adding the reaction heat from the reaction between acid and rock. They showed that the reaction heat shortens the acid penetration distance and suggested to consider the effect of reaction heat for more accurate prediction. Figure 1-3 shows the temperature distributions with and without reaction heat. Those analyitical models assume the constant fracture geometry and leakoff rate.

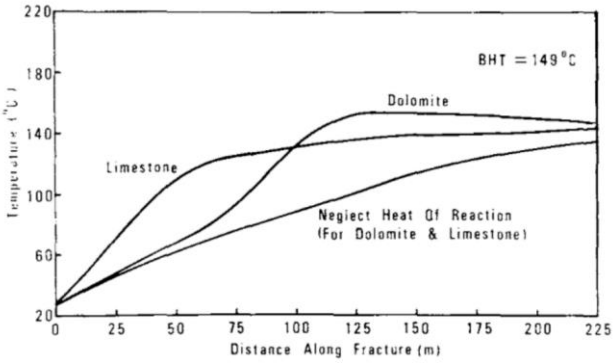

Figure 1-3 Temperature distribution in the fracture from Lee and Roberts (1980) model (reservoir temperature = 149C)

Settari (1993) developed a numerical acid fracturing model which solves for fracturing geometry, leakoff, heat transfer, and acid transport simultaneously. The model considered the effect of fluid type and wormholes. He took into account the wormhole effect on leakoff by comparing the leakoff experiment with and without wormholes. Also a temperature-dependent reaction rate of acid and reaction heat are considered in his

model. Using this numerical model, he showed that the heat of reaction has a significant effect on the temperature profile in the fracture.

Lyons et al. (2013) solved the fluid, heat, and mass transport numerically in a realistic fracture geometry. They showed that the effect of temperature stimulate the acid reaction and enlarge both the etched width and the pore volumes in matrix. Though their simulation can handle a realistic fracture geometry including the pore in matrix, their calculation is limited to the pore scale. It seems difficult to apply their method to estimate the acid penetration distance which requires the reservoir size scale simulation.

Guo et al. (2014) also developed the acid fracturing model which considered pressure and temperature dependence of heat reaction, while constant heat reaction are commonly used. They also took into account the effect of CO_2 produced as a reaction product. To compare with the result by Lee et al. (1980) as shown in Figure 1-3, Guo et al. used the similar inputs as Lee et al. showed, and observed that the deviation of temperature distribution caused by considering reaction heat from without reaction heat is much smaller (Figure 1-4) comparing with Lee et al. observation (Figure 1-3). One of the reasons for the deviation is that Guo et al. assumed the variable fracture length, leakoff velocity, and reaction heat. It is suggested that those simplified assumptions overestimate the heat reaction effect.

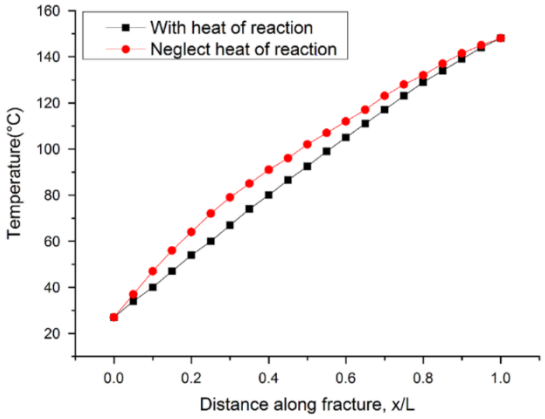

Figure 1-4 Temperature in the fracture from Guo et al. (2014) model (reservoir temperature = 149°C)

1.3.6. Acid Fracture Conductivity

After the acid injection process, the fracture will close due to the high formation stress. At this stage, roughness on the fracture faces prevents fracture from closing and create conductivity as shown in Figure 1-5.

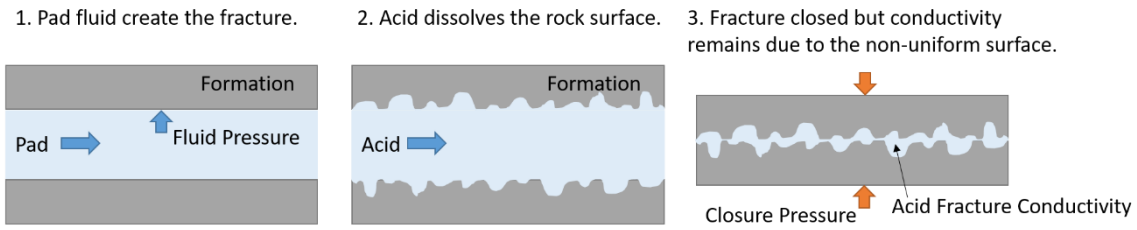

Figure 1-5 Process of conductivity creation in acid fracturing

The fracture conductivity after closure determines the effectiveness of fracturing stimulation. Fracture conductivity is defined as the product of the fracture permeability, k_f and the fracture width, w. Conductivity of acid fracture mainly depends on acid contact time, acid leakoff, rock mechanical properties, and formation heterogeneity (Gong 1998).

Conductivity of acid fracturing can be measured by experimental investigation which measures the pressure drop between acid etched rock surfaces. Numerous correlations have been published which relate the conductivity to some rock parameters from the experimental or numerical simulation results (Nierode and Kruk, 1973; Nasr-El-Din et al., 2008; Neumann, 2011; Deng et al., 2012). The most commonly used correlation is Nierode and Kruk (1973) model since it does not require statistical information about the fracture surface which is difficult to obtain. However, the heterogeneity in formation properties such as mineralogy, leakoff behavior, and permeability is the key to create conductivity. Deng et al. (2012) developed a correlation accounting for the heterogeneity in formation properties. Their correlation was developed by simulating the flow and acid transport between 10 ft by 10 ft two parallel plates. Since Deng et al. correlation considers the fracture surface heterogeneity, it requires information such as a ratio of limestone/dolomite and permeability correlation length. These two parameters can be obtained from well log and outcrop. Oeth et al. (2011) showed the procedure to obtain geostatistical parameters required in Deng's correlation and the field application of the correlation.

Most empirical correlations between conductivity, wk_f and the etched width, w_e have the same form as follows (Nierode and Kruk, 1973; Nasr-El-Din et al., 2008; Neumann, 2011; Deng et al., 2012):

$$wk_f = Aw_e^B \tag{1.11}$$

where A and B are constants. Equations for A and B depends on each correlations. Etched width, w_e is also known as ideal width, and it is defined as "width a fracture would have

based on the volume of rock dissolved by the acid, all other factors being neglected" (Schechter, 1991). Constants A and B in empirical correlations proposed to date are summarized by Schwalbert (2019).

1.3.7. Acid Fractured Well Performance

There are fewer studies about acid-fractured well performance comparing to the proppant-fractured well. Ben-Naceur and Economides (1989) developed a design model which couple the fracture propagation to the acid and heat transport. Their model allows us to design multiple fluid injections, and considered the influence of viscous fingering and wormholes. They showed a comparison of the various treatment schedule and fluid type. Ravikumar et al. (2015) applied the "Unified Fracture Design", which is a classic fracture design optimization method for proppant fracturing to acid fractured well. Aljawad et al. (2018a) performed the optimization of acid fracturing using an integrated acid fracture and productivity model. They examined the sensitivity of productivity to several parameters such as injection rate, fluid type, and pad volumes. Schwalbert (2019) developed an analytical estimate of fracture productivity based on Unified Fracture Design, and showed that the result from the analytical estimate is very close to the result of full simulation by using fully integrated acid fracturing simulator developed by Aljawad and Schwalbert (2019). The comparison results between analytical model and full simulation is illustrated in Figure 1-6.

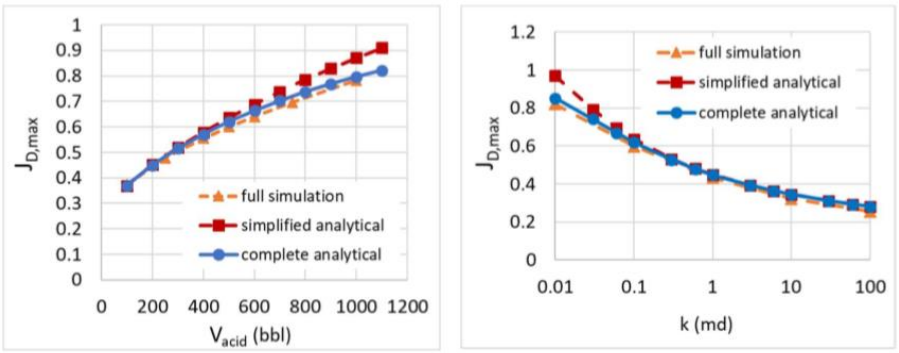

(a) (b)

Figure 1-6 Comparison of the analytical solution and the full simulation for various (a) acid injection volume and (b) formation permeability (Schwalbert, 2019)

1.3.8. Acid Fracturing Models

Several models describe acid fracturing have been developed to date. The improvement of acid fracturing models is summarized in this section.

The first acid fracturing model is an analytical solution to estimate the acid penetration distance which was proposed by Willimas and Nirode (1972). They applied Terrill's (1965) analytical solution for temperature distribution in the equi-distanced parallel walls to acid transport in the fracture. Roberts and Guin (1975) derived an analytical equation to calculate the apparent reaction rate constant to consider the finite reactivity at the fracture wall. And solved analytically.

Since 1980s, numerical models for acid fracturing were developed to consider a more complicated situation. Lo and Dean (1989) developed the numerical simulator for acid fracturing, which considers the fracture propagation, multiple stage injection, and non-Newtonian fluid. They used the fracture width equation fluid derived by Perkins and Kern (1961) for non-Newtonian, and obtained the fracture length to satisfy the material

balance. The detail of this procedure is discussed in Section 2.2 since the same approach is used in this study. Settari (1993) developed a 2D acid fracturing model that considers the effect of wormholes on leakoff using the experimental results. Settari also considered the temperature effect on acid fracturing, and showed the example acid fracture design.

Romero (1998) and Settari (2001) modeled the acid fracturing in 3D so that the fracture width also can be divided into several grids. Both concluded that conventional 2D models underestimate that the etched width and final conductivity, and 3D models should be used to predict acid fracturing. Though their approaches do not require the empirical parameter to estimate the diffusion of acid to the fracture surface because they discretized the fracture in the direction of fracture width, the velocity profile in the fracture is calculated from the Berman's analytical solution, which assumes the constant leakoff rate and uniform fracture width. It seems that their final conductivity is higher than 2D model due to these assumptions.

Oeth et al. (2013) developed a fully 3D acid fracturing model by solving the Navier-Stokes equation in the fracture. Wu et al. (2013) improved Oeth et al. (2013) model by incorporating the commercial fracture simulator and reservoir simulator. Though their model calculates the acid transport accurately with the velocity from the Navier-Stokes equation, the acid transport was solved only after the fracture propagation is finished. In reality, acid is injected and reacts with the fracture wall while the fracture is propagating.

Al Jawad (2018) developed a fully integrated acid fracturing model, which considers the fracture propagation, acid transport, and heat transport in the acid fracture in 3D. His model uses Berman's analytical solution for the velocity field in the fracture

as with Romero (1998) and Settari (2001), and calculates acid concentration during the hydraulic fracture is propagating. Al Jawad discussed that the acid penetration distance was overestimated in a non-coupled constant fracture geometry model. He also showed the temperature effect on the acid reactivity and diffusivity has a huge impact on the final fracture geometry and conductivity. Schwalbert (2019) improved Al Jawad (2018) model to consider the wormhole effect on the leakoff and added productivity model which can be used to optimize the stimulation. He also developed a matrix acidizing model and compared the productivity of acid fracturing and matrix acidizing. He showed that the wormhole effect is insignificant in acid fracturing treatments.

2. MODEL DEVELOPMENT

The numerical simulation model is developed to analyze acid fracturing in carbonate reservoirs. The model simulates fracture propagation, acid reaction with rock, pressure distribution, and heat transport. Temperature sensitive variables such as acid diffusivity, reaction rate, and the rheological parameters of fracturing fluid are a function of temperature. At the same time, the reaction heat generated from the acid-rock reaction affects the temperature of fluid. Pressure and temperature are computed not only in the fracture but also in the reservoir. Since the numerical simulator does not rely on the analytical solutions, the material balance is always satisfied during the fracture propagation. The wormhole propagation from the fracture wall is considered using Schwalbert (2019) model. In this chapter, the governing equations used in the model explained first. Then the structure of the numerical simulator is stated.

2.1. Rheology of Fluids

2.1.1. Rheological Properties of Fracturing Fluid

It is common to use high viscosity fluid to fracture a reservoir. Thus, the power law fluid is assumed in this research as a fracturing fluid. The rheological parameter largely depends on the temperature, and it should affect the fracture geometry and acid penetration distance. The following temperature modified constitutive equation (Cochrane, 1969) is used to express the temperature dependence of the rheology:

$$\tau = \mu_{app}\dot{\gamma} \tag{2.1}$$

$$\mu_{app} = K(T)|\dot{\gamma}|^{n-1} \tag{2.2}$$

where τ is shear stress, $\dot{\gamma}$ is shear rate, μ_{app} is apparent viscosity for power-law fluid, $K(T)$ is temperature modified consistency index, n is power-law exponent. The temperature modified consistency index $K(T)$ is a temperature dependent parameter as follows:

$$K(T) = m \cdot exp\left(\frac{\Delta H}{RT}\right)^{n} \tag{2.3}$$

where m is the constant coefficient, ΔH is flow activation energy and R is the gas constant.

2.1.2. Rheological Properties of Reservoir Fluid

The Elsharkawy model (1999) is selected to compute oil viscosity since the correlation is based on Middle East field data where carbonate reservoirs are common. The oil viscosity can be calculated from Eq.(2.4) and Eq.(2.5). Figure 2-1 shows the viscosity vs temperature relationship for oil which has an API gravity of 27.

$$X = 10^{[2.16924 - 0.02525\gamma_{API} - 0.68875 \log T]} \tag{2.4}$$

$$\mu_{od} = 10^{X} - 1.0 \tag{2.5}$$

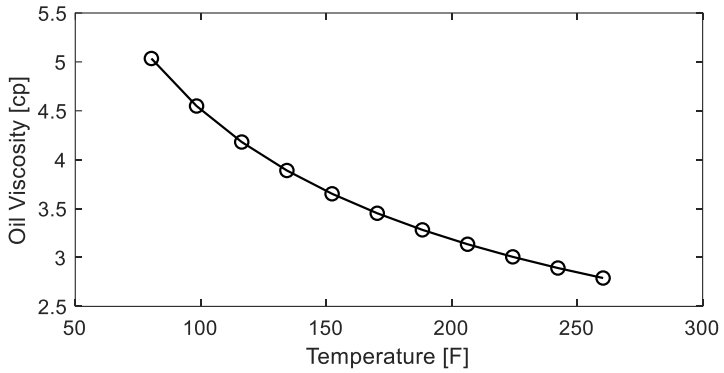

Figure 2-1 Oil Viscosity using Elsharkawy (1999) Correlation

2.2. Hydraulic Fracture Geometry

The one-dimensional fracture geometry calculation approach proposed by Lo and Dean (1989) was used in this study. Their approach is based on PKN model and can handle multiple fluid injection which has a different fluid properties. The reason for the selection is that all equations used to calculate fracture geometry, acid reaction, and heat transport calculation can be derived from the same assumptions, and thus material balance is satisfied through the fracture propagation process.

Lo and Dean (1989) proposed the procedure to calculate the fracture geometry when multiple power-law fluids are injected. They assumed leakoff volume does not affect the fracture width distribution, and calculated fracture width analytically from the material balance equation in the fracture without considering leakoff. The maximum width of the fracture for power-low fluid without considering leakoff, w_{max} is (Perkins, 1961):

$$w_{max}(x) = \left\{ \frac{128}{3\pi} \frac{(n+1)K(1-\nu^2)h_f}{E} \left[\frac{(2n+1)q_{inj}}{nh_f} \right] (X_f - x) \right\}^{\frac{1}{2n+2}} \qquad (2.6)$$

where ν is Poisson's ratio, h_f is the height of reservoir zone, E is Young's modulus, q_{inj} is injection rate, X_f is fracture length, x is the position along the fracture length direction, and all are in SI unit. Note that fracture length, X_f is unknown, and thus we first need to obtain X_f.

Fracture length, X_f is computed to satisfy both the material balance with leakoff and the fracture width calculated from the no-leakoff material balance equation. The actual material balance in the fracture is written as:

$$V_f = V_{injected} - V_{leakoff} \tag{2.7}$$

where V_f is volume of the fracture, $V_{injected}$ is total injection volume of fluid, and $V_{leakoff}$ is the total volume leaked off from the fracture. Those are calculated from the following equations.

$$V_f(X_f) = \frac{3\pi}{128}\frac{E}{K(1-\nu^2)(2n+3)}\left[\frac{nh_f}{(2n+1)q_{inj}}\right]^n w_{max,0}(X_f)^{2n+3} \tag{2.8}$$

$$V_{injected} = \int_0^t q_{inj}dt \tag{2.9}$$

$$V_{leakoff}(X_f) = 8h_f\int_0^{X_f}\int_0^t C_L(x,t)\sqrt{t-\tau(x)}\,dx \tag{2.10}$$

where $w_{max,0}$ is the maximum fracture width at the wellbore, $C_L(x,t)$ is the leakoff coefficient, and $\tau(x)$ is the time when the fracturing fluid arrive at the position x. Solving Eq.(2.6) for L and substituting the solution to Eq.(2.5), we obtain both fracture length and width.

2.2.1. Application of the Numerical Model

Fracture geometry is basically calculated by the procedure in the previous section, but one more procedure is required when the equation is applied in the numerical model. Since the numerical model is gridded along the fracture length direction, the fracture length should be adjusted to fit the gridding system. To do so, first we calculate fracture width and length by the analytical solution shown in the previous section, and then the length is changed to nearest grid face. Using the adjusted fracture length, the fracture width at the wellbore, $w_{max,0}(0)$ is calculated. The ratio of the adjusted fracture width to the fracture width first calculated is multiplied to all widths to satisfy the material balance. Since the fracture length will be modified to fit the gridding system, fine grids in x-direction are required to produce realistic fracture propagation, otherwise the propagation will be step wise.

2.3. Pressure and Velocity Distribution

Pressure and velocity distribution in the fracture and reservoir are computed separately. Those two domains are connected by the leakoff volume at the boundary.

2.3.1. Pressure and Velocity Distribution in the Fracture

Inside of the fracture, velocity distribution is first obtained by the material balance equation. Then, using the relationship between average velocity and pressure drop, pressure distribution is computed.

The velocity distribution in the hydraulic fracture is calculated to satisfy the material balance in the hydraulic fracture. The material balance equation in the fracture when timestep proceeds from t to $t + \Delta t$ in i-th grid block is:

$$\Delta q_{in,i}^{t+\Delta t} = \left(V_{f,i}^{t+\Delta t} - V_{f,i}^{t}\right) - q_{leak,i}^{t+\Delta t} \tag{2.11}$$

where $\Delta q_{in,i}$ is the net flux at i-th grid block. Figure 2-2 shows the material balance in the i-th grid block. Since the injection rate from the wellbore is known, the out flux from the left face in the 1st grid can be calculated. By repeating the same procedure until the tip of the fracture, we get the flow rate distribution in the fracture.

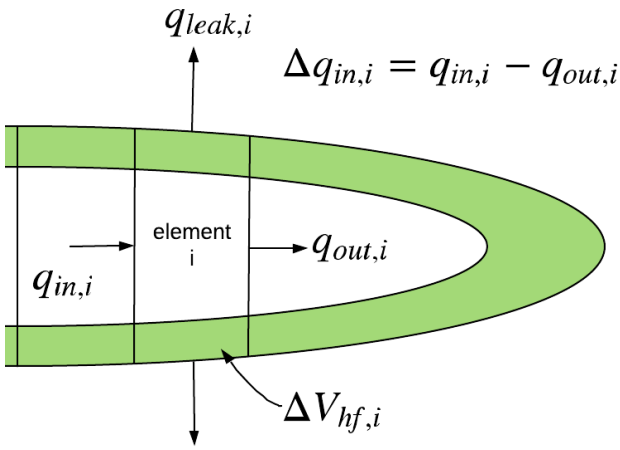

Figure 2-2 Schematic of material balance in hydraulic fracture

Pressure distribution in the fracture is obtained from the pressure drop between each block assuming that fluid pressure at the fracture tip is equal to the minimum horizontal stress. The pressure drop inside the fracture can be calculated from the relationship between the average velocity in the fracture and pressure drop as follows (Perkins and Kern, 1961):

$$\tilde{v}_f = 2h_f \left(\frac{n}{2n+1}\right)\left(\frac{\Delta p}{K\Delta x_{hf}}\right)^{\frac{1}{n}}\left(\frac{w}{2}\right)^{\frac{2n+1}{n}} \quad (2.12)$$

where Δx_{hf} is length of grid block in x direction in fracture.

2.3.2. Pressure and Velocity Distribution in the Reservoir

Pressure distribution in the reservoir domain is computed from a material balance equation for single phase slightly compressible fluid which is expressed as:

$$\nabla^2 p + \frac{\mu\phi c_t}{k}\frac{\partial p}{\partial t} = 0 \quad (2.13)$$

where c_t is the compressibility of reservoir fluid. Figure 2-3 shows the schematic of the calculation domain. All the boundary is no flow boundary except the boundary with hydraulic fracture. At the boundary with hydraulic fracture, the leakoff pressure is assigned to the boundary grids adjacent to the hydraulic fracture. The boundary conditions for pressure is expressed as follows:

$$\begin{aligned} p\left(x \le X_f, 0, t\right) &= p_{Lo}\,(x) \\ \left.\frac{\partial p}{\partial x}\right|_{(x \le X_f, 0, t)} &= 0 \\ \left.\frac{\partial p}{\partial x}\right|_{(0,y,t)} &= 0 \\ \left.\frac{\partial p}{\partial x}\right|_{(L_x,y,t)} &= 0 \end{aligned} \quad (2.14)$$

The initial condition is:

$$p(x, y, 0) = p_{res} \quad (2.15)$$

Eq.(2.13) is solved using finite volume method with Eq.(2.14) and Eq.(2.15).

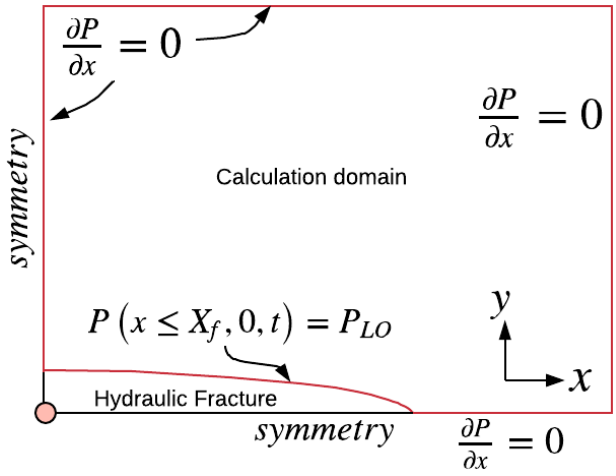

Figure 2-3 Schematic of pressure calculation domain and its boundary conditions

Once the pressure distribution in the reservoir is obtained, the velocity distribution can be computed. The velocity of the reservoir fluid is assumed to follow the Darcy's law.

$$\underline{v} = -\frac{k}{\mu}\underline{\nabla} p \tag{2.16}$$

2.4. Acid Transport and Reaction in the fracture

2.4.1. Mass Balance of Acid

The acid concentration profile in the fracture is solved numerically by following Settari's (1993) procedure. The difference from his model is that the model developed in this research assumes that calcite, dolomite and insoluble minerals exist in a rock. Mass balance equation in the fracture can be written as (assuming constant height)

$$-\frac{\partial(Cv_x)}{\partial x} - \frac{\partial\left(Cv_y\right)}{\partial y} + \frac{\partial}{\partial y}\left(D_e \frac{\partial C}{\partial y}\right) = \frac{\partial C}{\partial t} \tag{2.17}$$

where C is acid concentration, v_x and v_y are the fluid velocity in fracture length direction and width direction, D_e is the diffusion coefficient. To obtain boundary conditions at the

fracture surface, the relationship between the mass of acid transported to the fracture surface and the acid/rock reaction needs to be considered. The amount of acid arrive at the fracture surface is equal to the sum of leak-off acid and the reacted acid. Thus,

$$-\left(-f_l C_B v_l + D_e \frac{\partial C}{\partial y}\right)\Big|_{\frac{w}{2}} = (1-\phi) E_f \left(C_B - C_{eqm}\right)^m \qquad (2.18)$$

where f_l is the fraction of leaking acid with the fracture walls before entering into the formation, ϕ is porosity of matrix, E_f is reaction rate constant, C_B is the concentration at the fracture wall, and m is the reaction order of mineral.

The fraction of leaking acid with the fracture walls before entering into the formation, f_l represents the proportion of mass of acid reacts with the fracture walls to the total mass of acid arrives at the fracture walls by convection. The rest of acid leaks off into the formation, and contributes to create wormholes. For example, $f_l = 1$ means all acid arrives at the fracture surfaces by convection reacts with minerals at the fracture surfaces. On the other hand, $f_l = 0$ indicates that all acid leaks off into the formation and is consumed to create wormholes. Though f_l is commonly used in acid fracturing numerical models, the appropriate value for f_l is not known. In this study, $f_l = 0$ was used.

To solve Eq.(2.18) numerically, it is required to discretize the domain in the fracture width direction because the left hand side of Eq.(2.18) includes a derivative in width direction. However, we can eliminate a discretization in width direction by introducing the parametric apparent mass-transfer coefficient, which is introduced by Roberts and Guin (1974). The relationship between the concentration derivative in width direction and the parametric apparent mass-transfer coefficient, K_g is

$$K_g\left(\tilde{C} - C_B\right) = -D_e \left.\frac{\partial C}{\partial y}\right|_{\frac{w}{2}} \tag{2.19}$$

where $\tilde{C}$ is the average concentration. Substituting the equation into the mass balance equation gives,

$$-\frac{\partial(Cv_x)}{\partial x} - \frac{\partial\left(Cv_y\right)}{\partial y} + \frac{\partial}{\partial y}\left(-K_g\left(\tilde{C} - C_B\right)\right) = \frac{\partial C}{\partial t} \tag{2.20}$$

Integrating this in width direction gives

$$-\int_{-\frac{w}{2}}^{\frac{w}{2}} \frac{\partial(Cv_x)}{\partial x} dy - 2C_B v_l - 2K_g\left(\tilde{C} - C_B\right) = \int_{-\frac{w}{2}}^{\frac{w}{2}} \frac{\partial C}{\partial t} dy \tag{2.21}$$

And thus,

$$-\frac{\partial\left(\tilde{C}v_x w\right)}{\partial x} - 2C_B v_l - 2K_g\left(\tilde{C} - C_B\right) = \frac{\partial\left(w\tilde{C}\right)}{\partial t} \tag{2.22}$$

In Eq.(2.22), we have two unknowns, $\tilde{C}$ and C_B. To relate these, we consider the reaction at the fracture surface. The mass of acid arrives at the fracture surfaces is equal to the sum of the mass of acid reacts on the surface and the mass of acid leaks off. From this relationship, we get the following equation.

$$f_l C_B v_l + K_g\left(\tilde{C} - C_B\right) = (1 - \phi)E_f\left(C_B - C_{eqm}\right)^m \tag{2.23}$$

Isolating $\tilde{C}$ in Eq(2.23), we get

$$\tilde{C} = C_B + \frac{1}{K_g}\left[(1 - \phi)E_f\left(C_B - C_{eqm}\right)^m - f_l C_B v_l\right] \tag{2.24}$$

Substituting Eq.(2.24) into the mass balance equation [Eq.(2.22)], we get the non-linear equation with one unknown, C_B. The equations are solved with the boundary conditions and initial condition.

$$\tilde{C}(0,t) = C_{inj} \tag{2.25}$$

$$\tilde{C}\left(X_f,t\right) = 0 \tag{2.26}$$

$$\tilde{C}(x,0) = 0 \tag{2.27}$$

2.4.2. Parametric Apparent Mass-transfer Coefficient, K_g

The parametric apparent mass-transfer coefficient introduced in the previous section is calculated by the Nusselt number for acid transport, N_{Nu} and effective diffusivity coefficient, D_e as follows.

$$K_g = \frac{D_e N_{Nu}}{w} \tag{2.28}$$

The Nusselt number for acid transport is the dimensionless parameter which indicates the ratio of the mass-transfer by convection to conduction, and defined as (Settari, 1993):

$$N_{Nu} = -\frac{w}{\tilde{C} - C_B}\frac{\partial C}{\partial y}\Big|_{y=\frac{w}{2}} \tag{2.29}$$

Lo and Dean (1989) showed the Nusselt number for acid transport in laminar flow can be approximated using the Peclet number, N_{Pe} as follows:

$$N_{Nu} \approx \begin{cases} 4.10 + 1.26N_{Pe} + 0.02675N_{Pe}^2 \ (N_{Pe} < 10) \\ 2N_{Pe} \ (N_{Pe} \geq 20) \end{cases} \tag{2.30}$$

The Peclet number, N_{Pe} is the ratio of acid transport rate towards the fracture surface by convection to acid transport rate by diffusion:

$$N_{Pe} = \frac{\widetilde{w}}{2}\frac{v_l}{D_e} \tag{2.31}$$

where $\widetilde{w}$ is the average fracture width in height direction.

The calculation method of K_g for transient flow and turbulent flow is shown by Settari (1993). Since this research only focuses on the laminar flow, the calculation procedure for transient flow and turbulent flow are not discussed here.

2.4.3. Etched Width of Rock

Once the concentration profile is obtained, the etched volume of the fracture surface can be obtained from the following equation.

$$\Delta V_{acid} = M_{HCl}\Delta A_f \Delta t(1-\phi)E_f\left(C_B - C_{eqm}\right)^m \tag{2.32}$$

where M_{HCl} is molar mass of HCl. By introducing the dissolving power β, it is easy to convert the acid volume reacted to the mineral volume dissolved. Note that the volume of rock react with acid becomes $\frac{1}{1-\phi}$ times larger than actual volume of rock minerals.

$$\Delta V_{rock} = \frac{\beta}{\rho_{rock}(1-\phi)}\Delta V_{acid} \tag{2.33}$$

Dividing those volume changes of the rock by the area of the fracture, we obtain the etched width change during a small time Δt,

$$\Delta w_e = \frac{\Delta V_{rock}}{\Delta A_f} \tag{2.34}$$

This increment of the fracture width is called “ideal width”. Ideal fracture width is defined as “width a fracture would have based on the volume of rock dissolved by the acid, all other factors being neglected” (Schechter, 1991). Most empirical correlations for acid fracture conductivity are a function of ideal width.

2.5. Heat Transport

2.5.1. Wellbore Temperature Model

Though bottomhole temperature of acid is required to calculate the temperature distribution in subsurface, bottomhole temperature is usually unknown, on the other hand surface temperature is usually known. Thus, the interpretation of bottomhole temperature from surface temperature is required. The analytical solution proposed by Ramey (1962) is selected to calculate bottomhole temperature in this study. The Ramey's analytical equation is obtained by solving both total energy and mechanical energy equations simultaneously. To obtain analytical solution, the following assumptions were made.

1) Steady flow of a single-phase, incompressible fluid.
2) Geothermal temperature, T_e is linear function with depth.

$$T_e = az + b \tag{2.35}$$

where a is geothermal gradient [°F/ft], b is ambient temperauture [°F], z is depth [ft].

The temperature of liquid at the bottom hole is:

$$T_l(z,t) = az + b - aA + (T_0(t) + aA - b)\exp\left(-\frac{z}{A}\right) \tag{2.36}$$

$$A = \frac{q_{inj}\rho c_p\left(\lambda_{ma} + r_1 U_t f(t)\right)}{2\pi r_1 U_t \lambda_{ma}} \tag{2.37}$$

$$f(t) = -\ln\left(\frac{r_2}{2\sqrt{\alpha t}}\right) - 0.290 \tag{2.38}$$

$$\alpha = \frac{k_{ma}}{c_{ma}\rho_{ma}} \tag{2.39}$$

where $T_0(t)$ is surface temperature of injected fluid [°F], r_1 is the inside radius of tubing [ft], r_2 is the outside radius of casing [ft], t is time from start of injection [days], λ_{ma} is

matrix conductivity, c_{ma} is specific heat of matrix, ρ_{ma} is the density of matrix, U_t is overall heat transfer coefficient [Btu/(deg-ft^2-F)], and α is thermal diffusivity of the earth [ft^2/day]. If the wellbore thermal resistance is negligible, the overall heat transfer coefficient is much larger than matrix thermal conductivity. Thus, the last term in Eq.(2.37) is approximated to:

$$A = \frac{q_{inj}\rho c_p f(t)}{2\pi k_{ma}} \tag{2.40}$$

Eq.(2.40) is applied in the model since overall heat transfer coefficient is difficult to measure.

2.5.2. Heat Transport in the Fracture

The energy balance equation in the fracture is:

$$\frac{\partial}{\partial t}\left(\rho_f c_{p,f} w T\right) + \frac{\partial}{\partial x}\left(w\rho_f c_{p,f} T v_x\right) + \rho_f c_{p,f} T v_l - h_T(T_{res} - T) + H_{reaction} = 0 \tag{2.41}$$

where h_T is the heat transfer coefficient. The heat transfer coefficient, h_T can be calculated by the following equation:

$$h_T = \frac{N_{Nu}\lambda_f}{\widetilde{w}} \tag{2.42}$$

where N_{Nu} is the Nusselt number and λ_f is thermal conductivity of acid. Meyer (1989) showed that the Nusselt number for laminar flow of power law fluid between parallel plates is approximately constant over a wide range of power-law index, and a good representative value is $N_{Nu} = 4$. The diffusion in the fracture length direction is ignored since the effect of convection is much larger than conduction. The heat capacity and

density of the fracturing fluid are assumed to be constant. This one-dimensional partial differential equation is solved numerically with following initial and boundary conditions:

$$T(x,0) = T_{res}$$

$$T(0,t) = T_{inj}$$

where T_{inj} is the temperature at the fracture inlet.

2.5.3. Heat Transport in the Reservoir

The energy balance equation in the reservoir is:

$$\left(\phi\rho_f c_{p,f} + (1-\phi)\rho_r c_{p,r}\right)\frac{\partial T}{\partial t} + \nabla \cdot \left(-\lambda_{eff}\underline{\nabla} T + \rho_f c_{p,f}\underline{u}T\right) = 0 \qquad (2.43)$$

where λ_{eff} is effective thermal conductivity. Initial condition and boundary conditions are:

$$\begin{gathered} T\left(0 \le x \le L_f, 0, t\right) = T_{hf} \\ T(x,y,0) = T_{res} \\ \left.\frac{\partial T}{\partial x}\right|_{(0,y\neq 0,t)} = \left.\frac{\partial T}{\partial x}\right|_{(L_x,y,t)} = 0 \\ \left.\frac{\partial T}{\partial x}\right|_{(x,0,t)} = \left.\frac{\partial T}{\partial x}\right|_{(x,L_y,t)} = 0 \end{gathered} \qquad (2.44)$$

The temperature in the fracture is used as a boundary condition of the reservoir. Eq.(2.43) is discretized using the finite volume method, and solved for T with boundary conditions, Eq.(2.44).

2.6. Relationship between Acid Reaction and Temperature

Acid reaction and temperature affect each other. Coefficients related to the acid reaction, such as reaction rate constant, diffusivity of acid, and viscosity of acid are the temperature dependent. On the other hand, the reaction heat leads the temperature increase in the fracture. Thus, the temperature and acid transport calculation require iterative process.

2.6.1. Temperature Dependence of Reaction Rate Constant

The reaction rate constant and reaction order used in Section 2.4 depends on temperature. The reaction rate at certain temperature, E_f is obtained by the Arrhenius formula as:

$$E_f = E_{f0}\, exp\left(\frac{\Delta E}{RT}\right) \tag{2.45}$$

The values of E_{f0}, C_{eqm}, and m for calcite and dolomite are summarized in Table 2-1 (Economides, 2013).

Table 2-1 Coefficients appears in the Arrhenius formula for HCl and calcite/dolomite

Rock type	n_r	E_{f0} $\left[\frac{kgmol(HCl)}{m^2 s \frac{kgmol(HCl)}{m^3(acid\ solution)}^m}\right]$	$\frac{\Delta E}{R}$ $[K]$	C_{eqm} $[kgmol/m^3]$
Calcite	0.63	7.31×10^7	7.55×10^3	0
Dolomite	$\frac{6.32 \times 10^{-4} T}{1 - 1.92 \times 10^{-3} T}$	4.48×10^7	7.90×10^3	0

2.6.2. Temperature-dependent Diffusion Coefficient

The temperature dependent diffusion coefficient, D_e is calculated as follows (Perry, 1997):

$$D_e = D_{e,ref} \frac{T}{T_{ref}} \frac{\mu_{ref}}{\mu} \tag{2.46}$$

where T_{ref} is reference temperature and $D_{e,ref}$ is the diffusion coefficient at reference temperature.

2.6.3. Heat of Reaction

The reaction between acid and rock is exothermic reaction. The heat generated from the reaction affects the fluid temperature in the fracture. The heat of reaction can be obtained by summing up the standard generation enthalpy for all ions involved in the reaction. Though reaction heat is a function of pressure and temperature as shown by Guo

et al. (2014), constant values were used for simplicity. The heat of reaction between HCl and calcite or dolomite is (Al Jawad, 2018)

$$\Delta H^{\circ}_{r_{calcite}} = -7.5\ [kJ/mol\ H^{+}] = -205.7\ [kJ/kg - 100\%HCl] \quad (2.47)$$

$$\Delta H^{\circ}_{r_{dolomite}} = -6.9\ [kJ/mol\ H^{+}] = -189.2\ [kJ/kg - 100\%HCl] \quad (2.48)$$

2.7. Acid Fracture Conductivity

Unlike proppant fracturing, the conductivity evaluation for acid fracturing is difficult to calculate because too many parameters (e.g. acid reactivity, surface roughness, and mineral distribution) are involved. Nierode-Kruk (1973) and Deng et al. (2012) correlations were used to evaluate the conductivity for acid fracturing in this research. Both models have the same form of conductivity equation as follows:

$$wk_f = Ae^{B} \quad (2.49)$$

where A and B are constants, and those values depend on correlations. Coefficients for Nierode and Kruk (1973) model and Deng et al (2012) model are summarized in the following sections. Other common correlations are summarized by Schwalbert (2019).

2.8. Nierode and Kruk (1973) Model

The most popular acid fracturing empirical conductivity correlation is proposed by Nierode and Kruk (1973). Their correlation is developed from the experimental results using core samples which were fractured in tension to get rough fracture surface. Their correlation is:

$$A = \begin{cases} 1.476 \times 10^7 \exp\left[-0.001\{13.9 - 1.3\ln(S_{res})\}\sigma'_C\right] & S_{res} < 20000\ psi \\ 1.476 \times 10^7 \exp\left[-0.001\{3.8 - 0.28\ln(S_{res})\}\sigma'_C\right] & \text{otherwise} \end{cases} \quad (2.50)$$

$$B = 2.466 \quad (2.51)$$

where σ'_C is the effective confining stress [psi], S_{RES} is the rock embedment strength [psi]. This relationship is widely used because it does not require the parameters for fracture surface heterogeneity which is difficult to obtain. Though it is easy to apply, the effect of the heterogeneity of formation properties is crucial for fracture conductivity.

2.9. Deng et al. (2012) Model

Deng et.al. (2012) developed the numerical model which mimic acid fracturing process by creating the rough fracture surface and solving 3D Navier-Stokes equation for the flow between rough surfaces. The coefficient A shown in the following sections is calculated as:

$$A = \frac{\alpha \exp(-\beta\sigma'_C)}{w_e^B} \quad (2.52)$$

Their model has four cases depending on the mineralogy distribution and leakoff coefficient.

2.9.1. Permeability-Distribution-Dominant Cases with High Leakoff

Permeability distribution dominant case can be applied when the mineralogy distribution is relatively uniform. When the leakoff coefficient is $C_L \geq 0.004ft/\sqrt{min}$, coefficients can be calculated as follows:

$$A = 4.48 \times 10^9 \times [0.56\,\mathrm{erf}(0.8\sigma_D)]^3 \times \left[0.22\left(\lambda_{D,x}\sigma_D\right)^{2.8} + 0.01\left(\left(1-\lambda_{D,z}\right)\sigma_D\right)^{0.4}\right]^{0.52} \times \left\{1 + \left[1.82\,\mathrm{erf}\left(3.25\left(\lambda_{D,x}-0.12\right)\right) - 1.31\,\mathrm{erf}\left(6.71\left(\lambda_{D,z}-0.03\right)\right)\right]\sqrt{e^{\sigma_D}-1}\right\} \times \exp\{-(14.9 - 3.78ln\sigma_D - 6.81lnE)\sigma_C' \times 10^{-4}\} \quad (2.53)$$

$$B = 2.49 \quad (2.54)$$

2.9.2. Permeability-Distribution-Dominant Cases with Medium Leakoff

When the leakoff coefficient is about $C_L \approx 0.001\,ft/\sqrt{min}$ with uniform mineralogy distribution, coefficients can be calculated as follows:

$$A = 4.48 \times 10^9 \times [0.2\,\mathrm{erf}(0.78\sigma_D)]^3 \times \left[0.22\left(\lambda_{D,x}\sigma_D\right)^{2.8} + 0.01\left\{\left(1-\lambda_{D,z}\right)\sigma_D\right\}^{0.4}\right]^{0.52} \times \left\{1 + \left[1.82\,\mathrm{erf}\left(3.25\left(\lambda_{D,x}-0.12\right)\right) - 1.31\,\mathrm{erf}\left(6.71\left(\lambda_{D,z}-0.03\right)\right)\right]\sqrt{e^{\sigma_D}-1}\right\} \times \exp\{-(14.9 - 3.78ln\sigma_D - 6.81lnE)\sigma_C' \times 10^{-4}\} \quad (2.55)$$

$$B = 2.43 \quad (2.56)$$

2.9.3. Mineralogy-Distribution-Dominant Cases

When the mineralogy distribution is dominant factor and the leakoff coefficient is $C_L \geq 0.004ft/\sqrt{min}$, the coefficients in correlation are:

$$A = 4.48 \times 10^9 \times \left(0.13\mathrm{f}_{\mathrm{calcite}}^{0.56}\right)^3 \times \{1 + 2.97(1 - f_{calcite})^{2.02}\} \times (0.811 - 0.853f_{calcite}) \times \exp\{-(1.2\exp(0.952f_{calcite}) + 10.5E^{-1.823})\sigma_C' \times 10^{-4}\} \quad (2.57)$$

$$B = 2.52 \quad (2.58)$$

2.9.4. Competing Effects of Permeability and Mineralogy Distributions

In this case, both mineralogy and permeability distribution are assumed to have an influence on the fracture conductivity. The leakoff coefficient is $C_L \approx 0.001\ ft/\sqrt{min}$.

$$A = 4.48 \times 10^9 \times (0.1 f_{calcite}^{0.43} + 0.14\sigma_D)^3 \times \left\{1.2 + \left[erf\left(5\left(\lambda_{D,x} - 0.12\right)\right) - 0.6\, erf\left(3.5\left(\lambda_{D,z} - 0.03\right)\right)\right]\sqrt{e^{\sigma_D} - 1}\right\} \times exp\{-(53.8 + 18.9 ln\sigma_D - 4.58 lnE)\sigma_C' \times 10^{-4}\} \quad (2.59)$$

$$B = 2.52 \quad (2.60)$$

2.10. Productivity of Acid Fractured Reservoir

Once fracture conductivity is estimated, the productivity of an acid-fractured well can be calculated. The productivity simulator developed by Schwalbert (2019) was integrated to the acid fracturing model developed in this study. The productivity model computes the pressure distribution in three-dimensional reservoir in each time step assuming the pseudo-steady state (no flow boundary is used as a far field condition). The same equations for the pressure during acid fracturing (Eq. (2.13)) is used. The initial condition is:

$$p(x, y, 0) = p_{res} \quad (2.61)$$

The boundary conditions are:

$$\left.\frac{\partial p}{\partial x}\right|_{(L_x,y,t)} = \left.\frac{\partial p}{\partial x}\right|_{(0,y,t)} = \left.\frac{\partial p}{\partial x}\right|_{(x,0,t)} = \left.\frac{\partial p}{\partial x}\right|_{(x,L_y,t)} \quad (2.62)$$

$$p(0,0,t) = p_{wf}$$

The impact of fracture on productivity is added to the productivity calculation by converting conductivity into fracture permeability. Suppose we set the fracture grid block width as Δx_{hf}, then the permeability of the fracture is

$$k_f = \frac{k_f w}{\Delta x_{hf}} \tag{2.63}$$

This permeability is assigned into the grid blocks where fracture exist.

2.11. Architecture of Numerical Simulator

. The governing equations explained in the above sections are applied to the numerical simulator, which have two individual calculation domain; the acid fracture and reservoir. The schematics of two domains are illustrated in Figure 2-4 (a). Fracture propagation and acid concentration are calculated in the fracture domain, while the pressure and temperature calculation are calculated in both domains. When the calculation is implemented for both domains, only a quarter of the reservoir is simulated assuming the system is symmetry. As illustrated in Figure 2-4 (b), cross-sectional area of the hydraulic fracture domain is elliptical, while the reservoir domain is gridded with rectangles.

Since the temperature in reservoir change only close to the hydraulic fracture, temperature is calculated in a smaller domain than in the entire reservoir to reduce the computational time. Figure 2-5 illustrates the temperature calculation domain in reservoir.

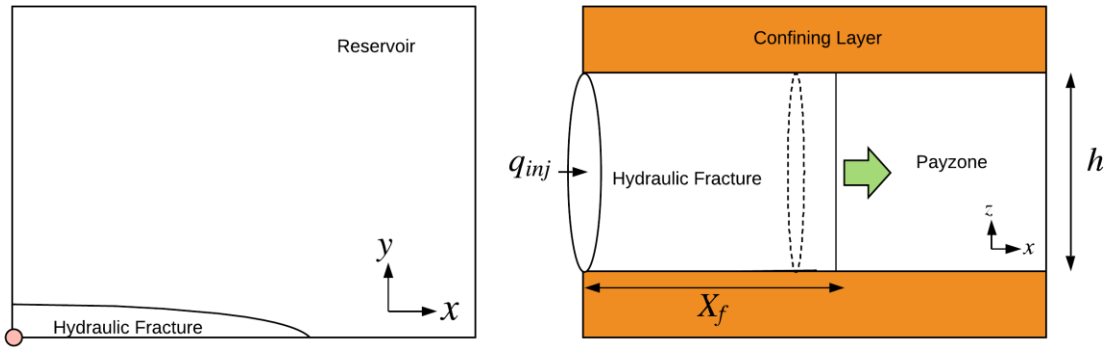

(a) Top view of the acid fractured reservoir

(b) Side view of the fracture domain

Figure 2-4 Schematics of calculation domain

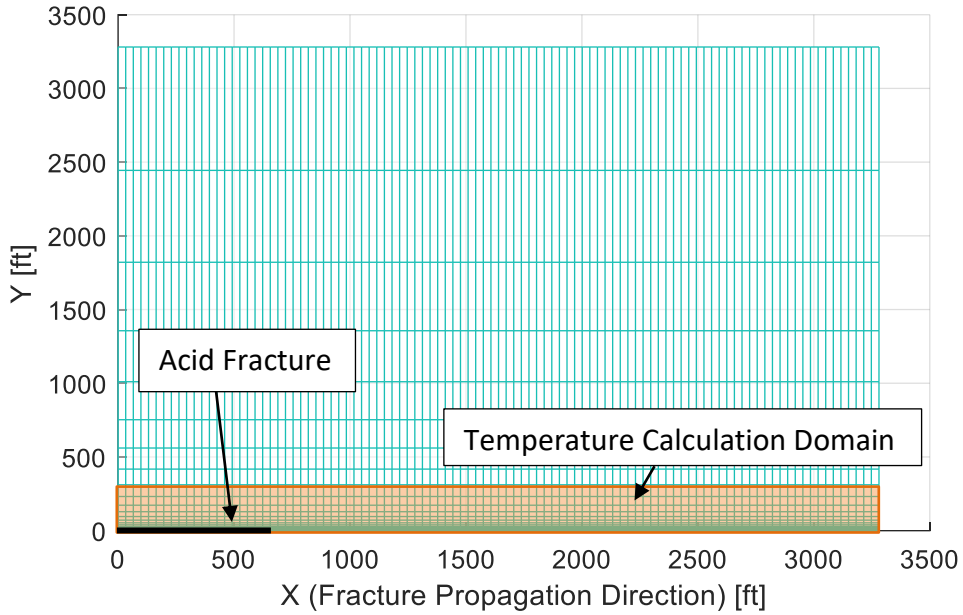

Figure 2-5 Mesh for reservoir domain

The calculation procedure can be divided into three phases. Figure 2-6 shows the flow chart of the numerical simulator developed in this research, and the key functions in the simulator are summarized in Table 2-2. The acid fracturing phase simulate the fluid

injection from the well by following the pumping schedule. The calculation for the fracture closure phase is similar to the acid fracturing phase except that the well is shut in. At the acid fracturing and closure phases, the model first calculates the temperature dependent fluid rheology parameters are for each grid blocks from the initial guess or the temperature from previous iteration step. Next, using this temperature modified consistency index, the fracture geometry, acid distribution along the fracture, and the temperature distribution are calculated. The temperature computed and the one used to calculate the rheology of fluid are compared, and if the error between those is small enough, the simulator starts to calculation for the next time step. Once the calculation is finished at the final time step, the model moves on to the evaluation of stimulation. Using the final acid penetration distance and etched widths, the fracture conductivity distribution and the productivity are calculated.

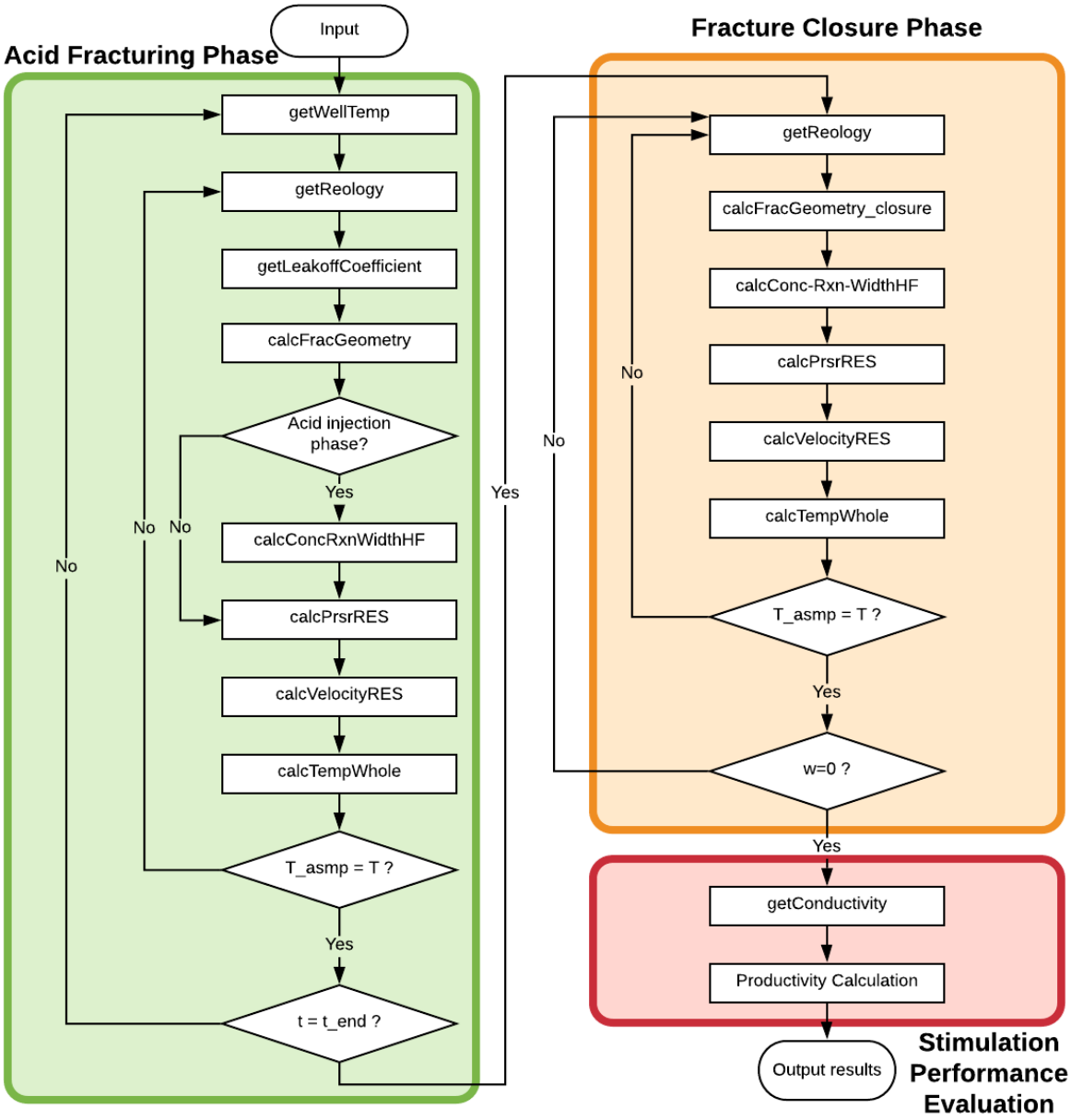

Figure 2-6 Flow chart of AcidFrac2D

Table 2-2 Key functions in AcidFrac2D

Function Name	Explanation
getWellTemp	Calculate injection temperature at bottom hole from surface temperature using Ramey ‘s (1962) equation.
getReology	Calculate temperature dependent consistency index and viscosity from input temperature.
getLeakoffCoefficient	Calculate leakoff coefficient. This function is called every timestep to consider pressure and wormhole length change.
calcFracGeometry	Compute fracture length and width along the fracture using Lo and Dean’s method (1989).
calcConcRxnWidthHF	Compute concentration profile along fracture, heat from reaction, and etched width of fracture.
calcPrsrRES	Compute pressure in the reservoir.
calcTempWhole	Compute temperature distribution in both the fracture and the reservoir.
calcConductivity	Calculate conductivity of the fracture using the Nierode-Kruk and Mou- Deng correlation.
calcVelocityWhole	Calculate velocity in the fracture and reservoir from pressure difference in each grid.

Table 2-3 Key functions in AcidFrac2D (continued)

Function Name	Explanation
funAcidFracJtransient3D_constpw_Jo	Calculate productivity without fracture to evaluate simulation efficiency. This function is coded by Schwalbert (2019) and a modification was made to consider pressure history during the acid fracturing treatment. Pseudo steady state and constant bottom hole pressure is assumed.
funAcidFracJtransient3D_constpw	Calculate productivity of the stimulated case. This function is coded by Schwalbert (2019) and modified to consider pressure history during the acid fracturing treatment. Pseudo steady state and constant bottom hole pressure is assumed.

3. VARIDATION OF THE ACID FRACTURING MODEL

3.1. Fracture Propagation

3.1.1. 2D Fracture Propagation Analytical Solutions

Numerical solution of 2D fracture propagation was validated with analytical solution. To derive analytical solution, the following simplified situation is considered.

1. Fluid is Newtonian (n=1).
2. Constant injection rate.
3. No leakoff.

In this simplified situation, the fracture width and length can be solved analytically from the fracture width equation [Eq.(2.6)] and the material balance equation [Eq.(2.7)]. Since the leakoff is ignored, the material balance equation [Eq.(2.7)] is simplified as follows:

$$V_f = V_{injected} \tag{3.1}$$

Thus, equating Eq.(2.8) and (2.9), we get

$$q_{inj} \cdot t_a = \frac{3\pi}{128} \frac{E}{K(1-\nu^2)(2n+3)} \left[\frac{nh_f}{(2n+1)q_{inj}}\right]^n \left\{w_{max,0}(X_f)\right\}^{2n+3} \tag{3.2}$$

where $w_{max,0}(X_f)$ is the maximum fracture width at the wellbore when fracture length is X_f. Substituting $n = 1$ and $x = 0$ in Eq.(2.6), we obtain

$$w_{max,0}(X_f) = \left\{\frac{256}{\pi} \frac{K(1-\nu^2)q_{inj}}{E} X_f\right\}^{\frac{1}{3}} \tag{3.3}$$

Substituting Eq.(3.3) into Eq.(3.2), and rearranging it, finally we get

$$X_f(t) = 0.6015\left(\frac{q'^3_{inj}G}{(1-\nu)Kh_f^4}\right)^{\frac{1}{5}} t^{\frac{4}{5}} \tag{3.4}$$

$$w_{max,0}(t) = 2.646\left(\frac{(1-\nu)q'^2_{inj}K}{Gh_f}\right)^{\frac{1}{5}} t^{\frac{1}{5}} \tag{3.5}$$

where q'_{inj} is the injection rate for only one wing. Those equations are very similar to the well-known PKN equation of no leakoff case, and the only difference is the constants (In PKN model, constants for $L(t)$ and $w_{max,0}(t)$ are 0.68 and 2.5, respectively).

Note that, even though the assumptions listed at the beginning of this section is the same as the assumptions used to derive the well-known PKN model for no leakoff case (Nordgren, 1972, Eq.20), PKN model for no leakoff case cannot be used for the validation of the fracture geometry model used in this study, and only the analytical solution derived here can be used. This is because the pressure-width relationship used to derive the analytical solution is different.

PKN model is derived from the following material balance equation in the fracture (Nordgren, 1972):

$$\frac{G}{64(1-\nu)\mu h_f}\frac{\partial^2 w^4}{\partial x^2} = \frac{\partial w}{\partial t} \tag{3.6}$$

On the other hand, the analytical solutions derived here [Eq.(3.4) and Eq.(3.5)] are originated from the pressure drop between two parallel plates and the relationship between shear stress and shear rate for non-Newtonian fluids (Perkins and Kern, 1961).

Pressure drop between parallel plates:

$$\frac{w}{2}\frac{\partial P}{\partial x} = \tau \tag{3.7}$$

Relationship between shear stress and shear rate for non-Newtonian fluids:

$$\tau = \mu_{app}\dot{\gamma} \tag{2.1}$$

where

$$\mu_{app} = K(T)|\dot{\gamma}|^{n-1} \tag{2.2}$$

3.1.2. Validation of Fracture Propagation

The fracture propagation model used in this research was validated with analytical solution derived in the previous section.

Table 3-1 shows the variables used for this calculation. Figure 3-1 shows the comparison between numerical and analytical solution. The fracture width and height of numerical solution perfectly matched with those of analytical solution.

Table 3-1 Input Data for Fracture Propagation Validation

Input Data	Values	Units
Pay zone height	100	ft
Consistency Index	0.0082	$psi/min^{0.5}$
n	1	-
Injection rate	20	bpm
Young's modulus	6×10^6	psi
Poisson's ratio	0.25	-
Minimum horizontal stress	4200	psi

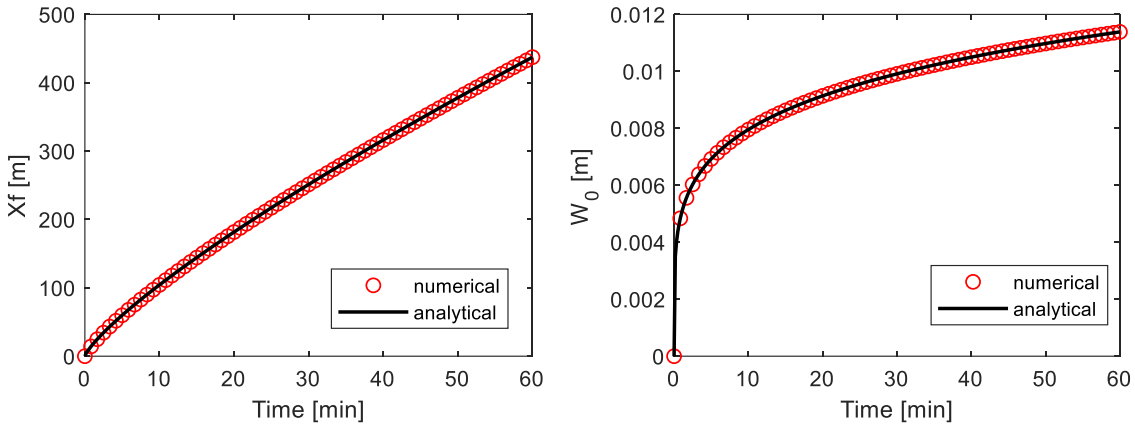

Figure 3-1 The validation for fracture propagation model

3.2. Validation of Acid Transport

The acid penetration distance along the fracture is validated using the analytical solution proposed by Nierode and Williams (1971). They showed the analytical solution for acid penetration distance in equi-spaced hydraulic fracture with constant leakoff. The solution is obtained by converting the analytical solution for heat transport proposed by Terrill (1965) to acid transport. The analytical solution is:

$$\frac{\tilde{C}}{C_{inj}} = \sum_{n=0}^{\infty} G_n \left(1 - \frac{N_{Re^*}}{N_{Re}}\xi\right)^{\frac{2\lambda_n^2}{3N_{Pe}}} \tag{3.8}$$

where $\tilde{C}$ is average concentration, C_{inj} is the injected acid concentration. N_{Re^*}, N_{Re}, and N_{Pe} are the Reynolds number in width direction, the Reynolds number in length direction, and Peclet number, and can be calculated as follows:

$$N_{Re^*} = \frac{v_l \tilde{w} \rho_a}{2\mu_a} \tag{3.9}$$

$$N_{Re} = \frac{q_{inj}\rho_a}{4h_f\mu_a} \tag{3.10}$$

$$N_{Pe} = \frac{v_l \widetilde{w}}{2D_e} \tag{3.11}$$

where ρ_a is the density of acid and ρ_a is the viscosity of acid.

λ_n is eigenvalues, and G_n is corresponding constants. Though Eq.(3.8) is the infinite series, if $0.001 < N_{Re^*} < 1$ and $N_{Pe} < 8$, only first six terms are required for calculation. λ_n and G_n are calculated by

$$\lambda_n = \sum_{i=0}^{3} g_{i,n} N_{Pe}^i + \sum_{i=1}^{2} h_{i,n} N_{Re^*}^i \tag{3.12}$$

$$G_n = \sum_{i=0}^{3} \bar{g}_{i,n} N_{Pe}^i + \sum_{i=1}^{2} \bar{h}_{i,n} N_{Re^*}^i \tag{3.13}$$

Coefficients appear in Eq. (3.12) and (3.13) are summarized in Table 3-2 and Table 3-3.

Table 3-2 Coefficients for Eq.(3.12) to calculate λ_n

n	$g_{0,n}$	$g_{1,n} \times 10$	$g_{2,n} \times 10^3$	$g_{3,n} \times 10^4$	$h_{1,n} \times 10^3$	$h_{2,n} \times 10^3$
0	1.68231	-2.26693	6.7544	-1.8408	6.7593	-4.6274
1	5.67053	-0.696	17.2931	-2.9304	1.0032	-3.4376
2	9.66842	-0.39587	10.7745	-0.5564	-5.7028	-0.4705
3	13.66772	-0.27662	7.9375	-0.1358	-9.15	-0.5668
4	17.6674	-0.21305	6.3431	-0.0373	-12.4496	-0.71169

Table 3-3 Coefficients for Eq.(3.13) to calculate G_n

n	$\bar{g}_{0,n} \times 10$	$\bar{g}_{1,n} \times 10^4$	$\bar{g}_{2,n} \times 10^4$	$\bar{g}_{3,n} \times 10^5$	$\bar{h}_{4,n} \times 10^4$	$\bar{h}_{5,n} \times 10^4$
0	9.10378	-2.38279	14.9298	-8.97017	-7.08188	-1.18392
1	0.53126	1.88909	-12.5375	8.13482	4.01538	0.35148
2	0.15272	0.39035	-1.6607	0.680785	1.0394	0.5154
3	0.06807	0.0733	-0.4172	0.111312	0.58639	0.141225
4	0.03739	0.01901	-0.1503	0.027559	0.35277	0.056322

To compare the numerical solution with the analytical solution explained above, several simplifications were made for the numerical model.

1. The fracture width and the leakoff rate are set as constant.
2. The reaction rate for the numerical model is set to a higher value than reality ($E_f = 0.1$) since the Nierode and Williams' solution assumes the infinite reactivity at the fracture wall.
3. The velocity profile is calculated by Berman's analytical solution for this validation though it is computed from the material balance equation in the fracture in the numerical model.

The input data used for validation are shown in Table 3-4. Figure 3-2 shows the comparison of solutions with various Peclet numbers. The numerical solution had a good match when the Peclet number is small, however, the error becomes larger as the Peclet number increase. This is because the numerical solution lump the Nusselt number in the fracture width equation, and thus it does not show S shape which can be observed in the analytical solution for high Peclet number. The same error was shown by Lo and Dean (1989) when they used the lumped Nusselt number in the fracture width direction.

Table 3-4 Input Data for Acid Transport Validation

Input Data	Values	Units
Fracture length	10	m
Fracture height	10	m
Fracture width	0.0254	m
Porosity of rock	0.15	-
Density of rock	2720	kg/m^3
Acid Type	HCl	-
Viscosity	100	cp
Acid concentration	15	wt%
Diffusivity	8×10^{-6}	m^2/s
Density of acid	1070	kg/m^3
Reaction rate constant	1	$\left[\frac{kgmol(HCl)}{m^2 s \frac{kgmol(HCl)}{m^3(acid\ solution)}^{m}}\right]$
Reaction order	1	-
Injection rate	0.0126/0.0252/0.1260/ 0.2520/0.6299/1.2598/ 1.7638	m^3/s

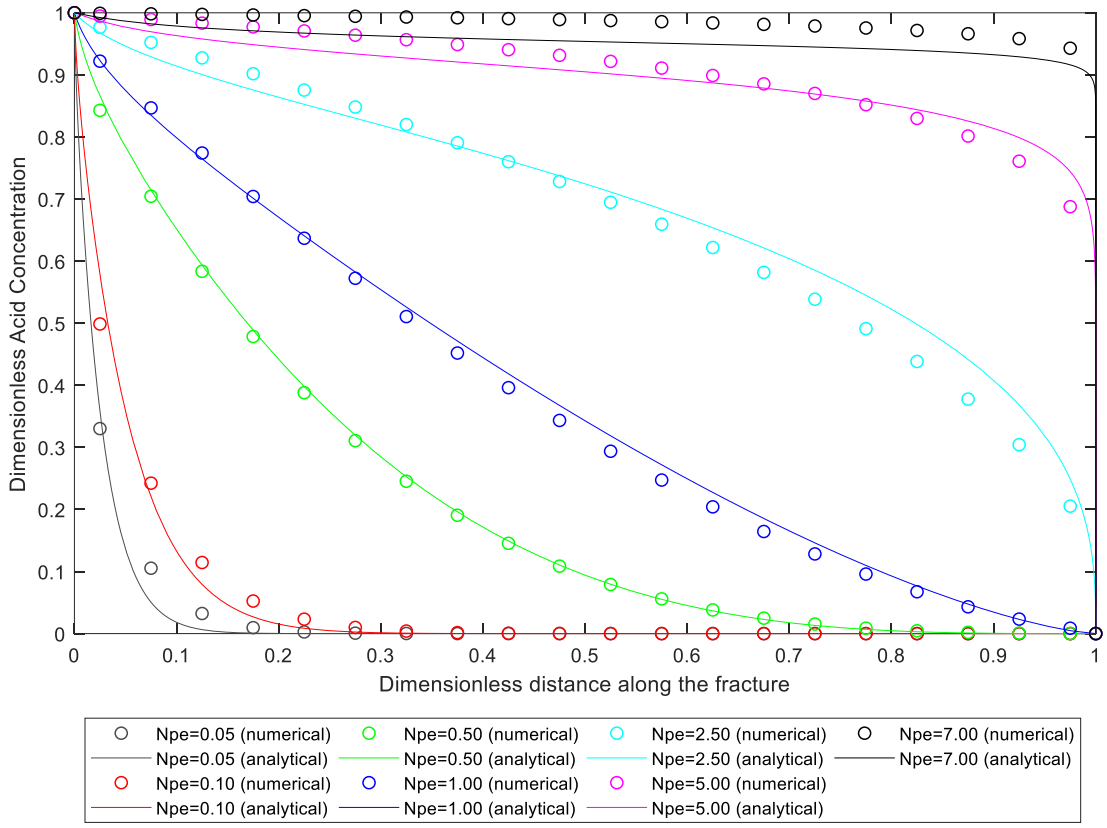

Figure 3-2 Comparison of numerical solution with Nierode (1971) analytical solution

It can be observed from Figure 3-2 that the acid does not reach the fracture tip when Peclet number is less than 1. Thus, the effective fracture length will be shorter than the dynamic fracture length if Peclet number is smaller than 1. Since the effective fracture length depends on the acid penetration distance, this case is called “reaction-rate limited”. On the other hand, when Peclet number is larger than 1, the effective fracture length is equal to the actual fracture length. In this case, the effective fracture length is called “fluid-loss limited”.

3.3. Ideal Fracture Width

The analytical equation for ideal fracture width is derived from the acid concentration equation Eq.(3.8), the velocity distribution, and stoichiometry relationship between acid and rock. The analytical equation for ideal width is (Schechter, 1992)

$$w_i = \frac{\chi C_{inj} q_{inj} t_a}{2(1-\phi) h_f L} \sum_{n=0}^{\infty} G_n \left(1 - \frac{N_{Re^*}}{N_{Re}} \xi\right)^{\frac{2\lambda_n^2}{3N_{Pe}}} \quad (3.14)$$

where χ is dissolving power of acid, t_a is the time of acid injection and C_0 is the injected acid concentration [kgHCl/m^3].

The results of analytical solution and numerical solution are compared using the input shown in Table 3-4 and the density of rock is 2720 kg/m^3. Figure 3-3 shows the comparison of etched width with various Peclet numbers. The dimensionless etched width is obtained by dividing the ideal width using the average value which is calculated by the following equation.

$$\widetilde{w_i} = \frac{\chi C_{\text{inj}} q_{inj} t_a}{2(1-\phi) h_f L} \quad (3.15)$$

According to Figure 3-3, the numerical solution had an agreement with the analytical solutions.

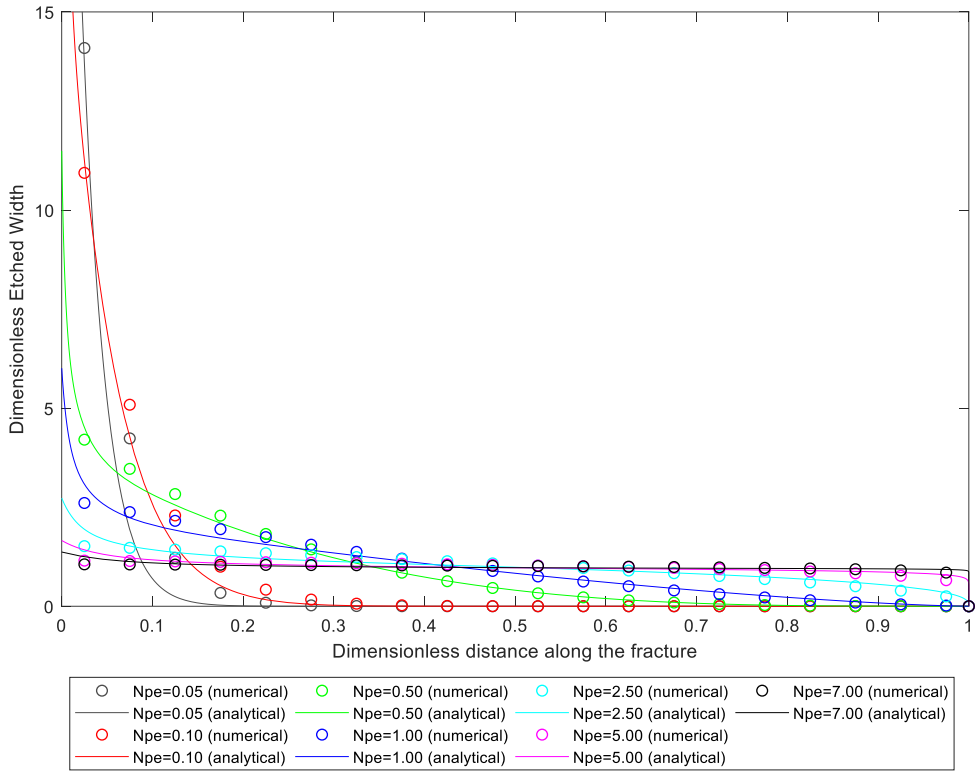

Figure 3-3 Dimensionless etched width comparison with analytical solution

The acid/rock reaction was also validated in terms of material balance of the acid. Since all acid is assumed to be spent to dissolve the fracture wall, the exact volume of dissolved rock can be expressed as:

$$V_{rock} = \frac{\chi}{1-\phi} q_{inj} t_a C_0 \tag{3.16}$$

Figure 3-4 shows the material balance error for both numerical and analytical solutions which is calculated by the following equation.

$$Error = \frac{\left| V_{rock} - V_{rock,exact} \right|}{V_{rock\_exact}} \tag{3.17}$$

The results show shows that both solutions conserve material balance rigorously.

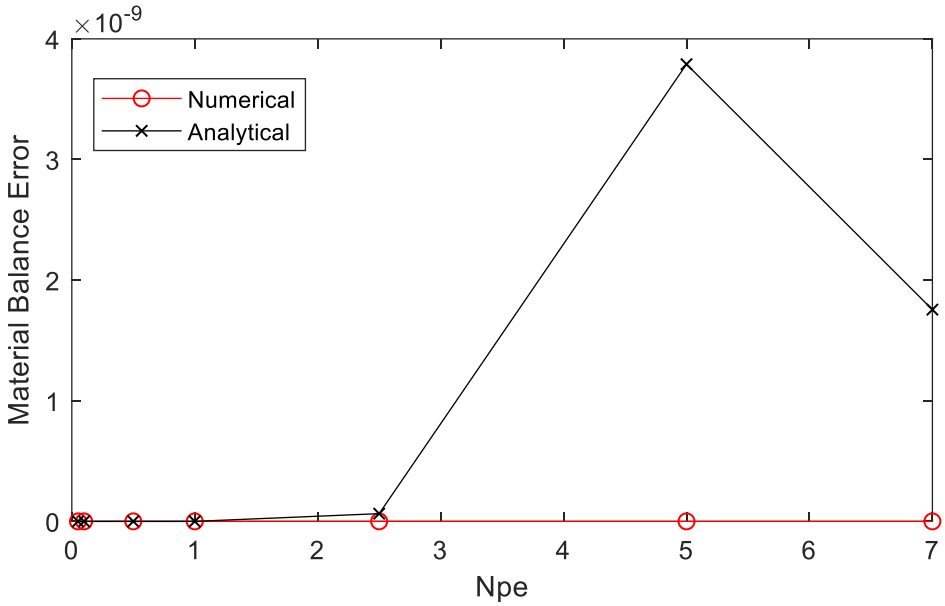

Figure 3-4 Material balance error of numerical and analytical solution

3.4. Heat Transport in Hydraulic Fracture

The temperature distribution in the fracture is validated using the analytical solution proposed by Terrill (1965). Since the principle of energy transport is exactly the same as acid transport, Eq.(3.4) can be used. The following assumptions were made to have the same condition as the analytical solution.

1. Fracture width and length constant along the fracture.
2. Fluid flow follows Berman's analytical solution and leakoff velocity is constant everywhere.

Input data used for the validation are summarized in Table 3-5. It should be noted that unrealistic values were used for thermal conductivity of acid and heat capacity of acid since the Terrill's analytical solution is valid only when $10^{-3} \leq N_{Re}^{*} \leq 1$, $N_{Re} \leq 1000$, and $N_{Pe} \leq 8$. Figure 3-5 shows the comparison between the analytical solution and the

numerical solution and it is concluded that the numerical solution had a good match with the analytical solution.

Table 3-5 Input data for temperature in the fracture validation

Input Data	Values	Units
Fracture length	10	m
Fracture height	10	m
Fracture width	0.0254	m
Viscosity of acid	100	cp
Density of acid	1070	kg/m^3
Acid type	HCl	-
Specific heat capacity of acid	10^{-3}	J/kg/K
Thermal conductivity of acid	10^{-4}	W/m/K
Injection Acid Temperature	298	K
Reservoir Temperature	373	K

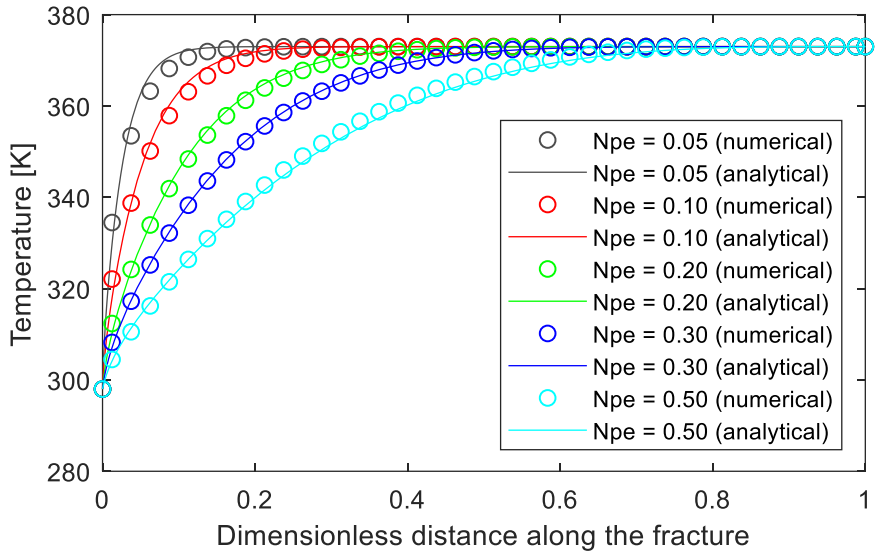

Figure 3-5 Temperature distribution validation in the hydraulic fracture

3.5. Pressure Distribution in Reservoir

The analytical solution for pressure in the reservoir was derived by solving one-dimensional transient pressure equation for slightly compressible fluid. To obtain the analytical solution, constant leakoff pressure from the fracture, constant reservoir properties and pseudo steady state (no flow boundary at the far field) are assumed. The material balance equation for slightly compressible fluid is

$$\frac{\partial^2 p}{\partial t^2} = \frac{c_t \phi \mu}{k} \frac{\partial p}{\partial t} \tag{3.18}$$

With boundary conditions

$$\begin{aligned} p(0,t) &= p_{LO} \\ \left.\frac{\partial p}{\partial x}\right|_{(\infty,t)} &= 0 \\ p(x,0) &= p_{res} \end{aligned} \tag{3.19}$$

where p_{LO} is the leakoff pressure from the hydraulic fracture. By solving this using Laplace transformation, we get

$$p_d = erfc\left(\frac{x}{2}\sqrt{\frac{c_t\phi\mu}{kt}}\right) \tag{3.20}$$

where p_d is the dimensionless pressure defined as follows:

$$p_d = \frac{p(x,t) - p}{p_{LO} - p_{res}} \tag{3.21}$$

The input data used for the validation are summarized in Table 3-6. The comparison between numerical and analytical solutions are shown in Figure 3-6. The numerical results matched with an analytical solution when the grid size is fine enough. In this case, the grid size Ny is 500.

Table 3-6 Input Data for Pressure Validation

Input Data	Values	Units
Reservoir length	1640	ft
Reservoir width	300	ft
Porosity	0.15	-
Viscosity	1	cp
Fluid compressibility	2.64×10^{-7}	1/psi
Permeability	1	md
Step size	1	minute
Calculation time	700	minutes

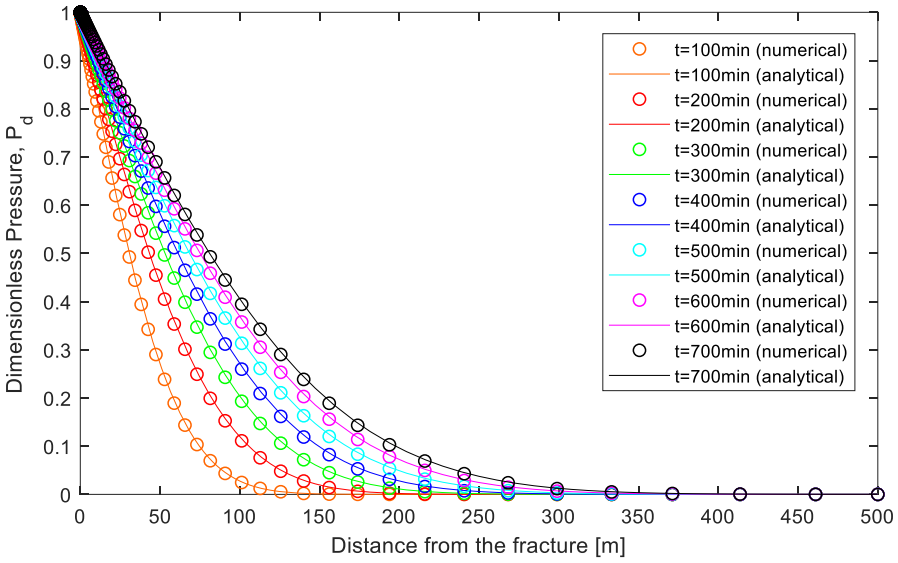

Figure 3-6 Comparison of the pressure distribution in the reservoir (Ny=500)

3.6. Heat Transport in Reservoir

Heat transport in the reservoir is validated when the temperature reached steady state. The following conditions are assumed to validate with analytical solution.

1. The fluid velocity inside the reservoir is constant.
2. The fluid temperature in the fracture and the reservoir temperature at far field are constant.
3. The temperature of the rock and the fluid are equal.
4. The fluid in the reservoir is Newtonian fluid.

The convection-diffusion equation at steady state is:

$$-\lambda_{ma}\frac{\partial^2 T}{\partial y^2}+\rho_f c_{p,f} u_y \frac{\partial T}{\partial y}=0 \qquad (3.22)$$

Boundary conditions are:

$$T(0) = T_{hf}$$
$$T(L_y) = T_{res} \tag{3.23}$$

where T_{HF} is fluid temperature in the fracture, T_{res} is the reservoir temperature, L_y is reservor length. The analytical solution for convection-diffusion problem is:

$$T = T_{hf} + (T_{res} - T_{hf}) \frac{e^{\frac{N_{Pe} y}{L_y}} - 1}{e^{N_{Pe}} - 1} \tag{3.24}$$

where N_{Pe} is Peclet Number, and it is equal to

$$N_{Pe} = \frac{\lambda_{ma}}{\rho_f c_{p,f} u_y L_y} \tag{3.25}$$

The values used for the validation are summarized in Table 3-7, and the comparison of analytical and numerical solutions is shown in Figure 3-7. From the comparison, it is proved that the numerical solution has enough accuracy.

Table 3-7 Input data for temperature validation

Input Data	Values	Unit
Reservoir length	500	m
Reservoir width	500	m
Porosity	0.15	-
Density of fluid	1073	kg/m^3
Density of rock	2720	kg/m^3
Specific heat capacity of fluid	4036.1	J/kg/K
Specific heat capacity of rock	1452.8	J/kg/K
Thermal diffusivity of fluid	0.6	W/m/K

Table 3-8 Input data for temperature validation (continued)

Input Data	Values	Unit
Thermal diffusivity of rock	1.57	W/m/K
Fluid temperature in the fracture	298	K
Reservoir temperature	373	K

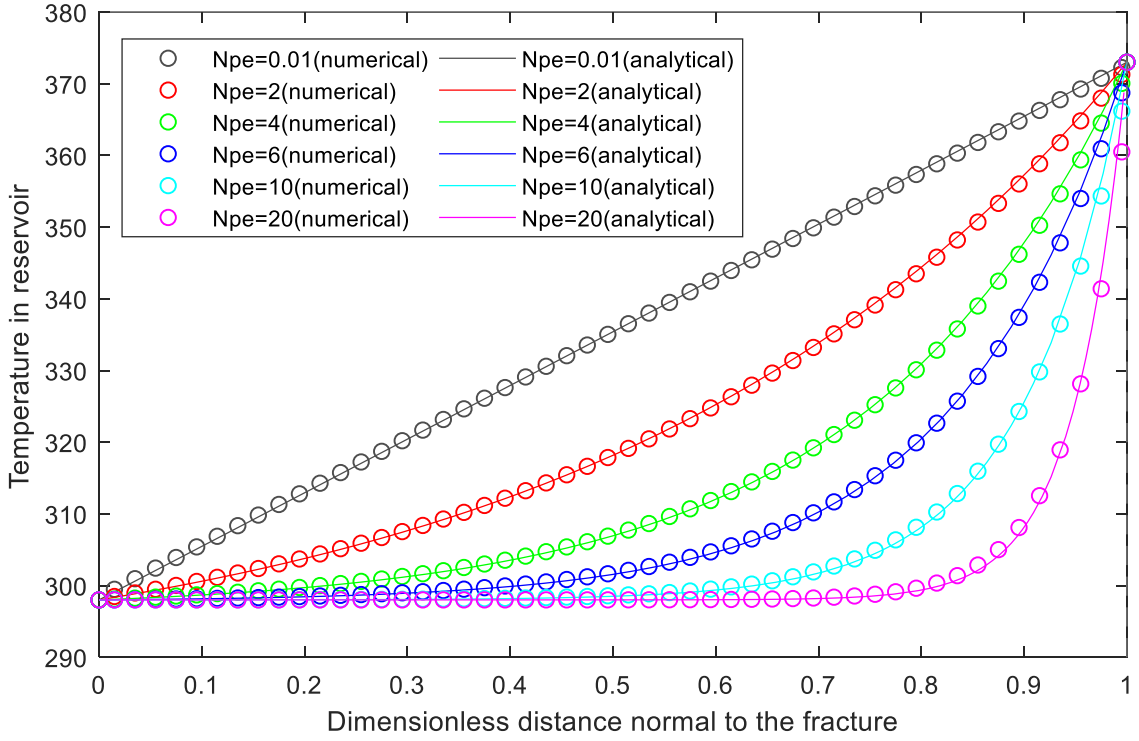

Figure 3-7 Temperature validation in reservoir with various Peclet Number

4. RESULTS AND DISCUSSIONS

In this chapter, the effect of the coupling acid fracturing model with the reservoir model is discussed. The input data shown in Table 4-1 was used for all simulations in this chapter unless otherwise specified. It should be noted that the pad and acid have the same fluid properties except the concentration of acid for simplicity. This is not oversimplification since it is common to prepare acid just by mixing acid into the pad fluid.

Table 4-1 Input data used in Chapter 4

Reservoir Properties		
Input Data	**Values**	**Unit**
reservoir domain size in x-direction	3281	ft
reservoir domain size y-direction	3281	ft
reservoir height	100	ft
total vertical depth	7000	ft
porosity	0.15	-
permeability	0.1	md
formation anisotropy in xy direction	1	-
formation anisotropy in xz direction	1	-
reservoir pressure	4000	psi
min horizontal stress	6000	psi
Young's modulus	4.00E+06	psi
Poisson's ratio	0.25	
density of rock	2598.8	kg/m3
wellbore pressure	2000	psi
oil formation volume factor	1.3	-
compressibility	1.00E-05	1/psi
inner casing radius	3.5	inch
outer casing radius	3.188	inch
geothermal gradient	-0.01	K/ft
ambient temperature	298.15	K
Injection temperature at surface	300.15	K
wellbore radius	0.3281	ft

Table 4-2 Input data used in Chapter 4 (continued)

Temperature dependent properties		
Input Data	**Values**	**Unit**
reservoir temperature	373.15	K
specific heat capacity of acid	4184	J/kg/K
specific heat capacity of rock	960	J/kg/K
thermal conductivity of acid	0.6	W/m/K
thermal conductivity of rock	3	W/m/K
API gravity of oil	27	degree
reference temperature for viscosity	298.15	K
Acid properties		
Input Data	**Values**	**Unit**
injection acid concentration	0.15	weight fraction
leak-off reaction fraction	0	
power-law exponent	0.55	
consistency index	0.0208	$lbf\text{-}s^n/ft^2$
reference temperature for consistency index	302	K
coefficient in the consistency index	1490.75	-
density of acid	848.954	kg/m^3
diffusion coefficient	8.00E-10	m2/s
reference temp for diffusion coefficient	302.15	K
Geostatistical Properties on Fracture Surface		
Input Data	**Values**	**Unit**
normalized standard deviation	0.7	
normalized x correlation length	0.7	
normalized x correlation length	0.005	
Acid Wormholing Parameters		
wormhole model	Schwalbert (2019)	
$PV_{bt,opt,core}$	0.5	
$v_{i,opt,core}$	2	cm/min
d_{core}	1	inch
ϵ_1	0.53	
ϵ_2	0.63	
d_{rep1}	3	ft
d_{rep2}	1	ft
Pumping Schedule		
Input Data	**Values**	**Unit**
Volume of pad	360	bbl
Volume of acid	360	bbl
Injection rate	40	bpm

4.1. The Effect of Coupling with Reservoir on Temperature Distribution

Most numerical acid fracturing models published are not coupled with reservoir model. The analytical solution proposed by Whitsitt and Dysart (1970) is commonly used to consider the heat from reservoir. (Lee 1980; Guo 2014; Al Jawad 2018). Moreover, the fracture geometry transient effect is commonly ignored for simplicity.

However, it should not be appropriate to use uniform reservoir properties especially in carbonate reservoir, and thus the leakoff should be calculated at each location numerically. Moreover, the fracture width change and propagation should affect heat transport since when the fracture width is smaller, the reservoir temperature conducts to the fracturing fluid more easily. To investigate the effect of the numerical approach to obtain reservoir temperature and fracture geometry transient effect, two different approaches were compared. Approach 1 is the simplified approach commonly used in acid fracturing literature, and Approach 2 is the approach used in this study. The differences between these two approaches are listed below, and the schematic of each approach is shown in Figure 4-1.

Approach 1 – Conventional acid fracturing and temperature model

1. The velocity profile in the fracture is calculated by an analytical model (Berman, 1956).
2. The fracture propagates with time as explained in Section 3.1, but use constant averaged width throughout the fracture.

3. The heat from reservoir is computed by an analytical solution (Whitsitt and Dysart, 1970).

Approach 2 – Acid fracturing and temperature model developed in this study.

1. Velocity profile is numerically simulated from the mass balance equation.
2. Fracture width changes as function of location and time.
3. Heat transfer from the reservoir is numerically simulated.

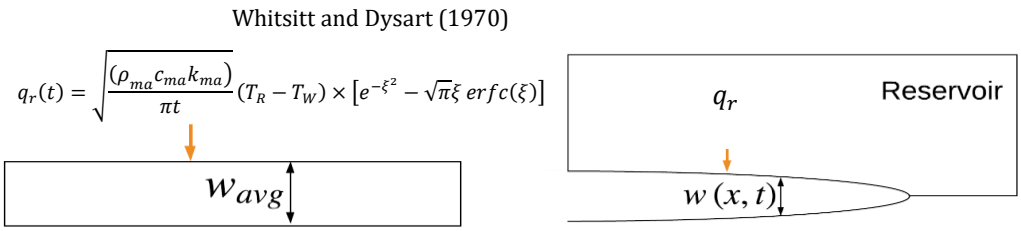

Figure 4-1 Schematic for each approach

Figure 4-2 shows the comparison of temperature distribution after 18 minutes injection and Figure 4-3 shows the concentration distribution after the injection. In both figures, the red line shows the approach used in this study (Approach 2), and black line shows the approach used commonly in other acid fracturing literature (Approach 1). As shown in Figure 4-2 and 4-3, the temperature and acid concentration distribution of both approaches do not have a significant difference.

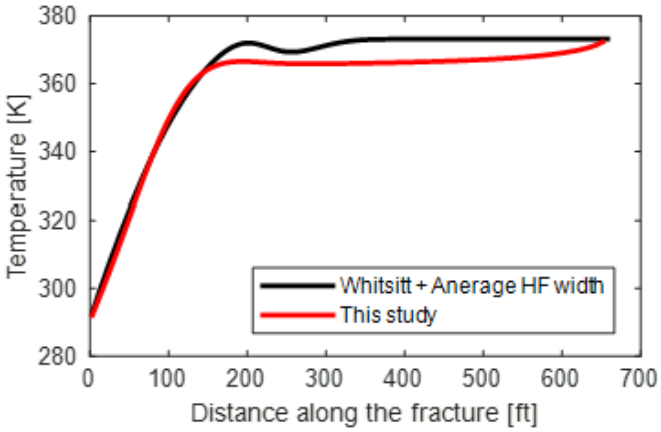

Figure 4-2 Comparison of the temperature along the fracture using two different models.

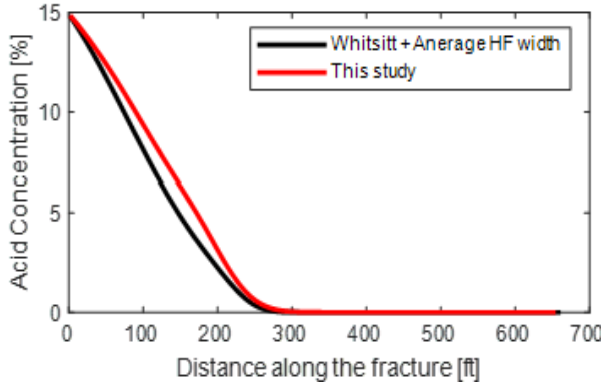

Figure 4-3 Comparison of acid concentration profile using two different models.

Also, the final distribution of most temperature-sensitive parameters in acid fracturing, namely viscosity and diffusivity of acid are shown in Figure 4-4 and Figure 4-5. Their trend follows that of temperature, and they did not have a huge difference.

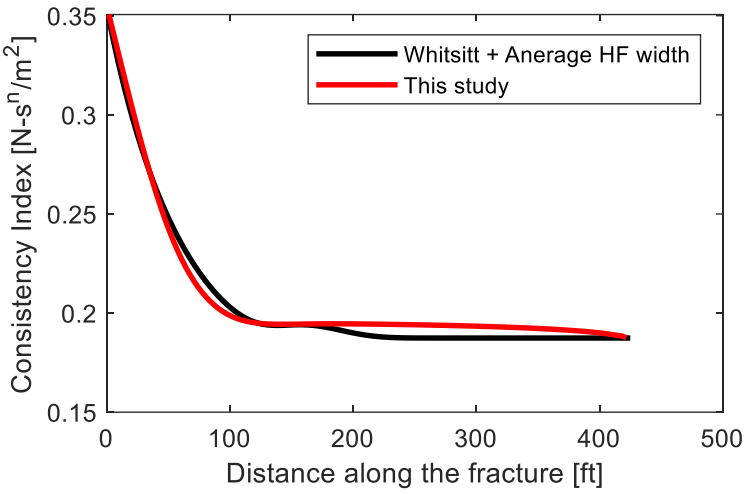

Figure 4-4 Comparison of consistency index using two different models.

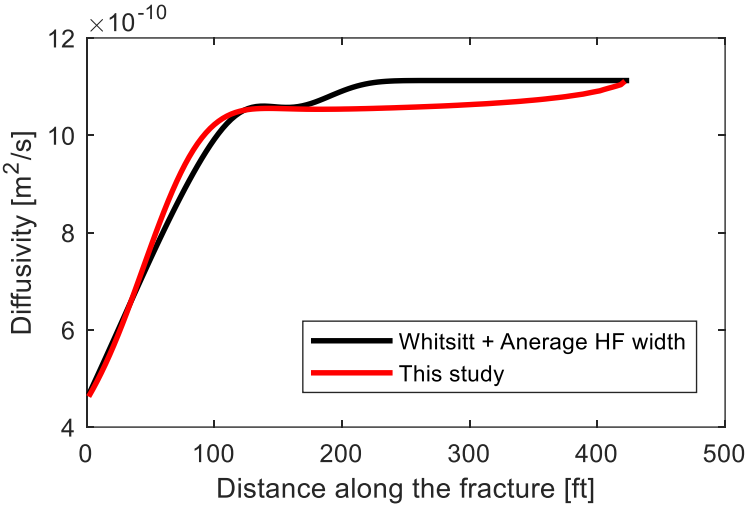

Figure 4-5 Comparison of diffusivity of acid using two different models.

However, the final conductivity from the approach used in this study (Approach 1) is much lower than the old approach (Approach 2). This difference can be explained from the assumptions of the two approaches. First, the old approach (Approach 1) uses Berman's equation to obtain the velocity. Since Berman's solution assume that the fracture

width is constant, and all fluids injected leaks off. This assumption allows the leakoff velocity to be faster than the approach used in this study. Due to these simplified assumptions, more acid will be delivered at the fracture wall if the simplified approach (Approach 1) was used. It can be concluded that the simplified approach (Approach 1) overestimate fracture etched width and thus the productivity.

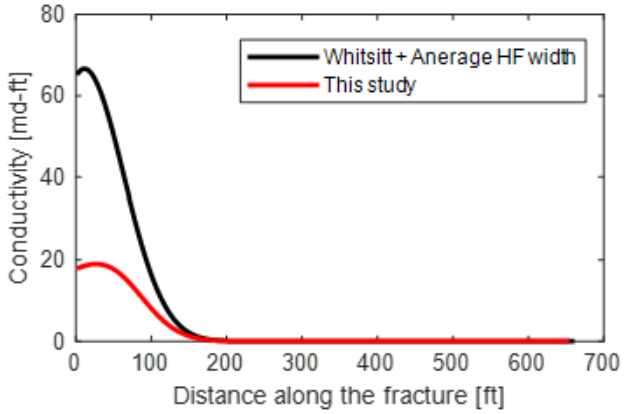

Figure 4-6 Comparison of conductivity distribution using two different models

4.2. Effect of Wormholes

One of the difficulties in acid fracturing is to control acid reaction at the entrance of the fracture. When acid leaks off from the fracture surface, it creates wormholes. Since wormholes are highly permeable, fluid leakoff increases significantly. It is a common problem during acid fracturing that the leakoff becomes significant and the fracture closes during the injection and the stimulation becomes matrix acidizing. To identify the significance of the leakoff close to the entrance, the simulator was run with and without wormhole effect.Figure 4-7 shows leakoff rate distribution along the fracture with

wormhole effect, and each line indicates the distribution at different times. It can be seen from the figure that the leakoff rate increases at the fracture entrance due to the wormhole propagation, while the rest of the domain follows Carter's leakoff. Figure 4-8 shows the leakoff rate change with time at the grid block which is located at the entrance of the fracture. As shown in Figure 4-8, it was observed that the leakoff rate significantly increases once the acid starts to create wormholes. The leakoff rate at the fracture inlet reaches a peak at 12 minutes and starts decreasing after that. The reason for the decrease of leakoff rate from 12 minutes is due to the slowdown of wormhole propagation. Wormholes first efficiently propagate since leakoff velocity is above the optimum interstitial velocity. However, after 12 minutes, the velocity becomes below the optimum velocity and wormhole propagation rate decreases. It is the key to successful acid treatment to keep fracturing pressure high enough at the time when the leakoff coefficient at the entrance becomes maximum.

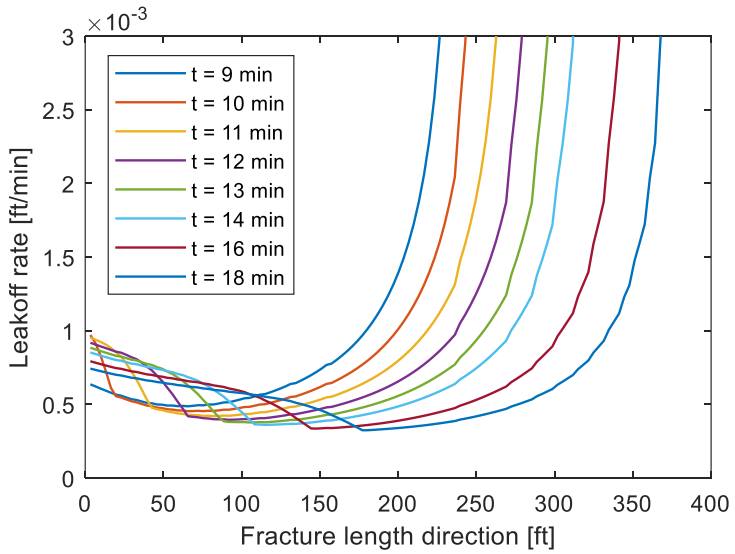

Figure 4-7 Effect of wormhole propagation on leakoff rate distribution with wormhole effect (Acid injection starts from 9 min)

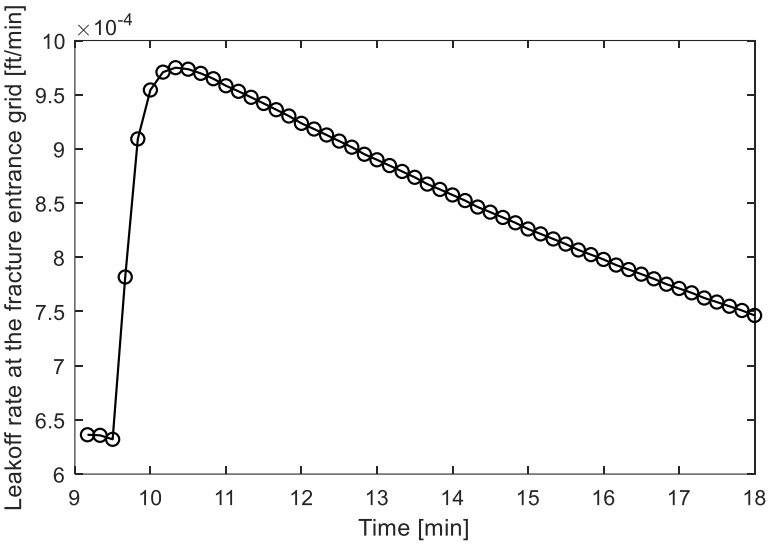

Figure 4-8 Leakoff coefficient change with time at the fracture inlet

Figure 4-9 shows the acid concentration distribution in the fracture, and Figure 4-10 shows the etched width profile after the injection. Both graphs show the distribution after 18 minutes of injection. The acid penetration distance does not differ significantly due to the existence of wormholes in this case, but it affects the ideal width distribution at the entrance of the fracture. The etched width distribution is larger at the entrance when wormhole effect is considered. Since the leakoff velocity will be faster due to wormholes, more acid and rock reaction can occur where the wormholes are propagating.

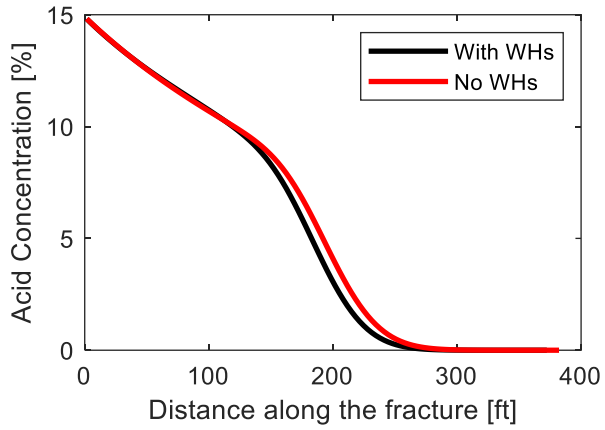

Figure 4-9 Acid concentration distribution comparison between with and without wormholes

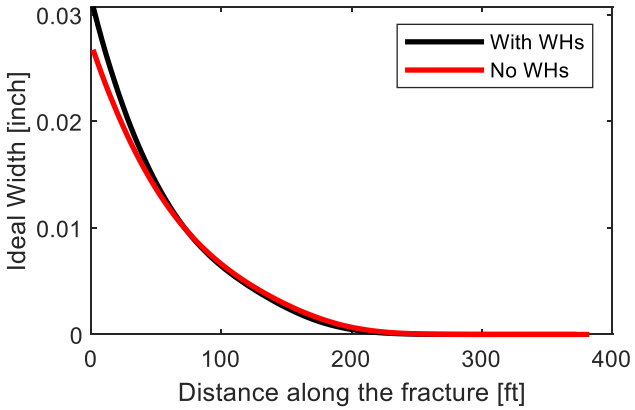

Figure 4-10 Ideal width comparison between with and without wormholes

5. CONCLUSIONS

5.1. Conclusions

The numerical simulation model for acid fracturing which considers fracture propagation, acid and heat transport was developed. The features of the model are the followings:

1. The model includes complex leakoff due to pressure and temperature change with time and wormhole propagation.
2. Material balance and energy balance in both fracture and reservoir are computed numerically using finite volume method. Unlike most of the acid fracturing model proposed, the fracture width variation in time and space are considered when the temperature in the fracture is calculated.
3. After the fluid injection, the fracture closure is simulated, and the final conductivity distribution and productivity are calculated.

Using the model developed, the effect of coupling of reservoir to acid fracturing model was investigated. From this study, the following conclusions were made:

1. The analytical equations for heat from the reservoir used in literature overestimates the final acid fracture conductivity, and thus the productivity. To include the fracture geometry variation in time and space and to couple with the reservoir thermal model is important to estimate final conductivity more accurately.

2. The wormhole effect was added and the distribution of leakoff coefficient was reasonable. It can be extended to simulate the fracture closure due to the huge fluid loss from wormholes.

5.2. Future Works

The followings should be pointed out as future works:

1. The model ignores the fracture height direction. Since one of the objectives of hydraulic fracturing is to create the vertical permeability, the height growth of fracture should also be considered. By replacing PKN model to P3D model, the height growth can be considered.
2. When hydrochloric acid and carbonate minerals react, CO_2 is generated, and it assists the pressure maintenance. However, the model developed in this study does not consider the effect of CO_2. This phenomenon should be added to simulate a more realistic condition.
3. The reservoir model coupled in the study is only for single phase slightly compressible fluid, and thus it cannot be applied for a gas reservoir. The model should be extended to the use for gas reservoir and multiple phase reservoir.
4. The fracture conductivity developed by Deng et al. was used to calculate the fracture conductivity. It can consider the effect of calcite and dolomite, however, recent experimental study shows that not only calcite and dolomite but also insoluble minerals affect the final fracture conductivity because they can hold the

conductivity after the fracture closure. Their effect should be added to the empirical acid fracture conductivity correlation.

5. Generally, carbonate reservoirs have natural fractures, and wormholes are created when the acid is injected. In this context, the assumption that the acid fracture propagates as a planner crack and acid mainly flow through the acid fracture is doubtful. More investigation should be done on the relationship between fracture propagation and fluid flow in naturally fractured carbonate reservoir.

REFERENCES

Akbar, M. V. (2000). A snapshot of carbonate reservoir evaluation. *Oilfield Review 12 (4)*, 20–21.

Al Jawad, M. S. (2018). *Development of a Fully Integrated Acid Fracture Model. PhD Dissertation.* College Station, TX: Texas A&M University.

Aljawad, M. S. (2018). Guidelines for Optimizing Acid Fracture Design Using an Integrated Acid Fracture and Productivity Model. *Society of Petroleum Engineers*, doi:10.2118/191423-18IHFT-MS.

Aljawad, M. S. (2018). Temperature and Geometry Effects on the Fracture Surfaces Dissolution Patterns in Acid Fracturing. *Society of Petroleum Engineers*, doi:10.2118/190819-MS.

Aljawad, M. S. (2019). Optimizing Acid Fracture Design in Calcite Formations: Guidelines Using a Fully Integrated Model. *Society of Petroleum Engineers*, doi:10.2118/198912-PA.

Ben-Naceur, K. &. (1989). Design and Evaluation of Acid Fracturing Treatments. *Society of Petroleum Engineers*, doi:10.2118/18978-MS.

Cochrane, G. (1969). *A Numerical Solution for Heat Transfer to Non-Newtonian Fluids with Temperature-Dependent Viscosity for Arbitrary Conditions of Heat Flux and Surface Temperature.* Oregon State University.

Convection in Porous Media Third Edition. (n.d.).

Deng, J. M. (2012). A New Correlation of Acid-Fracture Conductivity Subject to Closure Stress. *Society of Petroleum Engineers*, doi:10.2118/140402-PA.

Economides, M. J.-E. (2013). *Petroleum Production Systems, second edition.* Upper Saddle River, NJ: Prentice Hall.

Jianchun Guo, H. L. (2014). Effects of acid–rock reaction heat on fluid temperature profile in fracture during acid fracturing in carbonate reservoirs . *Journal of Petroleum Science and Engineering*, https://doi.org/10.1016/j.petrol.2014.08.016.

Kalfayan, L. (2008). *Production Enhancement with Acid Stimulation 2nd Edition.* Tulsa, Oklahoma: PennWell Corporation.

Khristianovic, S. a. (1955). Formation of Vertical Fractures by Means of Highly Viscous Liquid. *World Petroleum Congress*, 570-586.

Lee, M. H. (1980). Effect of Heat of Reaction on Temperature Distribution and Acid Penetration in a Fracture. *Society of Petroleum Engineers*, doi:10.2118/7893-PA.

Lo, K. K. (1989). Modeling of Acid Fracturing. *Society of Petroleum Engineers*, doi:10.2118/17110-PA.

Lyons, J. N.-E.-D. (2013). A Novel Model for Fracture Acidizing with Important Thermal Effects. *Society of Petroleum Engineers*, doi:10.2118/167158-MS.

Malalasekera, H. K. (2007). *An Introduction to Computational Fluid Dynamics THE FINITE VOLUME METHOD Second Edition.* Pearson Education.

McDuff, D. S. (2010). Understanding Wormholes in Carbonates: Unprecedented Experimental Scale and 3-D Visualization. *Society of Petroleum Engineers*, doi:10.2118/134379-MS.

Middleman., R. H. (1965). Power-Law Flow through a Packed Tube. *Ind. Eng. Chem. Fundamen.*, doi: 10.1021/i160016a011.

Mou, J. C. (2013). The Mechanism of Leakoff Reduction of Clean Self-Diversion Acid in Acid Fracturing. . . *International Petroleum Technology Conference*, doi:10.2523/IPTC-16720-MS.

Nierode, D. E. (1971). Characteristics of Acid Reaction in Limestone Formations. *Society of Petroleum Engineers*, doi:10.2118/3101-PA.

Nordgren, R. P. (1972). Propagation of a Vertical Hydraulic Fracture. *Society of Petroleum Engineers*, doi:10.2118/3009-PA.

Oeth, C. H. (2011). Characterization of Small Scale Heterogeneity to Predict Acid Fracture Performance. *Society of Petroleum Engineers*, doi:10.2118/140336-MS.

Oeth, C. V. (2013). Acid Fracturing: Fully 3D Simulation and Performance Prediction. *Society of Petroleum Engineers*, doi:10.2118/163840-MS.

Perkins, T. K. (1961). Widths of Hydraulic Fractures. *Society of Petroleum Engineers*, doi:10.2118/89-PA.

Perry, R. H. (1997). *Perry's Chemical Engineers' Handbook Seventh Edition.* The McGraw-Hill Companies, Inc.

R.M.Terrill. (1965). Heat transfer in laminar flow between parallel porous plates. *International Journal of Heat and Mass Transfer*, 1491-1497.

Ramey, H. J. (1962). Wellbore Heat Transmission. *Society of Petroleum Engineers*, doi:10.2118/96-PA.

Ravikumar, A. M.-P. (2015). Optimization of Acid Fracturing with Unified Fracture Design. *Society of Petroleum Engineers*, doi:10.2118/177486-MS.

Robertson, E. C. (1988). *Thermal Properties of Rocks.* United States Department of the Interior Geological Survey.

Romero, J. G. (1999). Three-Dimensional Transport in Acid Fracturing Treatments: Theoretical Development and Consequences for Hydrocarbon Production. *Society of Petroleum Engineers*, doi:10.2118/39956-MS.

Schwalbert, M. P. (2019). *Comprehensive Analysis of Acid Stimulation in Carbonate. PhD dissertation.* College Station, TX: Texas A&M University.

Settari, A. (1985). A New General Model of Fluid Loss in Hydraulic Fracturing. *Society of Petroleum Engineers*, doi:10.2118/11625-PA.

Settari, A. (1993). Modeling of Acid-Fracturing Treatments. *Society of Petroleum Engineers*, doi:10.2118/21870-PA.

Settari, A., Sullivan, R. B., & Hansen, C. (2001). A New Two-Dimensional Model for Acid-Fracturing Design. *Society of Petroleum Engineers*, doi:10.2118/74142-PA.

Shepherd, M. (2009). *AAPC Memoir 91 Oil Field Production Geology.* AAPG.

Terrill, R. (1965). Heat Transfer in Laminar Flow between Parallel Porous Plates. *Int. J. Heat Mass Transfer*, 1491-1497.

W. Ahr, D. A. (2005). Confronting the carbonate conundrum. *Schlumberger Oilfield Review*, 18-29.

Whitsitt, N. F. (1970). The Effect of Temperature On Stimulation Design. *Society of Petroleum Engineers*, doi:10.2118/2497-PA.

Williams, B. B. (1979). *Acidizing Fundamentals.* Dallas, TX: Society of Petroleum Engineers of AIME.

Wu, X. H. (2013). Integrated 3D Acid Fracturing Model for Carbonate Reservoir Stimulation. *Offshore Technology Conference*, doi:10.4043/24362-MS.